Prentice, SJ, Ashall, C, Mazzali, PA, Zhang, J-J, James, PA, Wang, X-F, Vinko, J, Percival, SM, Short, L, Piascik, A, Huang, F, Mo, J, Rui, L-M, Wang, J-G, Xiang, D-F, Xin, Y-X, Yi, W-M, Yu, X-G, Zhai, Q, Zhang, T-M, Hosseinzadeh, G, Howell, DA, McCully, C, Valenti, S, Cseh, B, Hanyecz, O, Kriskovics, L, Pal, A, Sarneczky, K, Sodor, A, Szakats, R, Szekely, P, Varga-Verebelyi, E, Vida, K, Bradac, M, Reichart, DE, Sand, D and Tartaglia, L

SN 2016coi/ASASSN-16fp: an example of residual helium in a type Ic supernova?

http://researchonline.ljmu.ac.uk/9493/

Article

Citation (please note it is advisable to refer to the publisher's version if you intend to cite from this work)

Prentice, SJ, Ashall, C, Mazzali, PA, Zhang, J-J, James, PA, Wang, X-F, Vinko, J, Percival, SM, Short, L, Piascik, A, Huang, F, Mo, J, Rui, L-M, Wang, J-G, Xiang, D-F, Xin, Y-X, Yi, W-M, Yu, X-G, Zhai, Q, Zhang, T-M, Hosseinzadeh, G, Howell, DA, McCully, C, Valenti, S, Cseh, B, Hanyecz, O,

Monthly Notices
of the
ROYAL ASTRONOMICAL SOCIETY

MNRAS **478,** 4162–4192 (2018)
Advance Access publication 2018 May 11

doi:10.1093/mnras/sty1223

SN 2016coi/ASASSN-16fp: an example of residual helium in a type Ic supernova?

S. J. Prentice,[1⋆] C. Ashall,[1,2⋆] P. A. Mazzali,[1,3] J.-J. Zhang,[4,5,6] P. A. James,[1] X.-F. Wang,[7] J. Vinkó,[8,9,10] S. Percival,[1] L. Short,[1] A. Piascik,[1] F. Huang,[7] J. Mo,[7] L.-M. Rui,[7] J.-G. Wang,[4,5,6] D.-F. Xiang,[7] Y.-X. Xin,[4,5,6] W.-M. Yi,[4,5,6] X.-G. Yu,[4,5,6] Q. Zhai,[4,5,6] T.-M. Zhang,[11] G. Hosseinzadeh,[12,13] D. A. Howell,[12,13] C. McCully,[12,13] S. Valenti,[14] B. Cseh,[8] O. Hanyecz,[8] L. Kriskovics,[8] A. Pál,[8] K. Sárneczky,[8] Á. Sódor,[8] R. Szakáts,[8] P. Székely,[15] E. Varga-Verebélyi,[8] K. Vida,[8] M. Bradac,[14] D. E. Reichart,[16] D. Sand[17] and L. Tartaglia[18]

[1] *Astrophysics Research Institute, Liverpool John Moores University, IC2, Liverpool Science Park, 146 Brownlow Hill, Liverpool L3 5RF, UK*
[2] *Department of Physics, Florida State University, Tallahassee, FL 32306, USA*
[3] *Max-Planck-Institut für Astrophysik, Karl-Schwarzschild-Str 1, D-85748 Garching, Germany*
[4] *Yunnan Observatories (YNAO), Chinese Academy of Sciences, Kunming 650216, China*
[5] *Key Laboratory for the Structure and Evolution of Celestial Objects, Chinese Academy of Sciences, Kunming 650216, China*
[6] *Center for Astronomical Mega-Science, Chinese Academy of Sciences, 20A Datun Road, Chaoyang District, Beijing 100012, China*
[7] *Physics Department and Tsinghua Center for Astrophysics (THCA), Tsinghua University, Beijing 100084, China*
[8] *Konkoly Observatory, Research Centre for Astronomy and Earth Sciences, Budapest, Konkoly-Thege út 15-17, 1121, Hungary*
[9] *Department of Optics and Quantum Electronics, University of Szeged, Dóm tér 9, Szeged 6720, Hungary*
[10] *Department of Astronomy, University of Texas at Austin, 2515 Speedway, Austin, TX 78712-1205, USA*
[11] *National Astronomical Observatories of China (NAOC), Chinese Academy of Sciences, Beijing 100012, China*
[12] *Las Cumbres Observatory, 6740 Cortona Dr. Suite 102, Goleta, CA 93117, USA*
[13] *University of California, Santa Barbara, Department of Physics, Broida Hall, Santa Barbara, CA 93111, USA*
[14] *Department of Physics, University of California, Davis, CA 95616, USA*
[15] *Department of Experimental Physics, University of Szeged, Dómtér 9, Szeged 6720, Hungary*
[16] *University of North Carolina 269 Phillips Hall, CB #3255 Chapel Hill, NC 27599, USA*
[17] *Department of Astronomy/Steward Observatory, 933 North Cherry Avenue, Room N204, Tucson, AZ 85721, USA*
[18] *Department of Astronomy and The Oskar Klein Centre, AlbaNova University Center, Stockholm University, SE-106 91 Stockholm, Sweden.*

Accepted 2018 May 4. Received 2018 May 4; in original form 2017 September 11

ABSTRACT

The optical observations of Ic-4 supernova (SN) 2016coi/ASASSN-16fp, from ∼2 to ∼450 d after explosion, are presented along with analysis of its physical properties. The SN shows the broad lines associated with SNe Ic-3/4 but with a key difference. The early spectra display a strong absorption feature at ∼5400 Å which is not seen in other SNe Ic-3/4 at this epoch. This feature has been attributed to He I in the literature. Spectral modelling of the SN in the early photospheric phase suggests the presence of residual He in a C/O dominated shell. However, the behaviour of the He I lines is unusual when compared with He-rich SNe, showing relatively low velocities and weakening rather than strengthening over time. The SN is found to rise to peak ∼16 d after core-collapse reaching a bolometric luminosity of $L_{\rm p}\sim3\times10^{42}$ erg s^{-1}. Spectral models, including the nebular epoch, show that the SN ejected 2.5–4 M$_\odot$ of material, with ∼1.5 M$_\odot$ below 5000 km s^{-1}, and with a kinetic energy of (4.5–7) × 10^{51} erg. The explosion synthesized ∼0.14 M$_\odot$ of ^{56}Ni. There are significant uncertainties in $E(B-V)_{\rm host}$ and the distance, however, which will affect $L_{\rm p}$ and $M_{\rm Ni}$. SN 2016coi exploded in a host similar to the Large Magellanic Cloud (LMC) and away from star-forming regions. The properties of the SN and the host-galaxy suggest that the progenitor had $M_{\rm ZAMS}$ of 23–28 M$_\odot$ and was stripped almost entirely down to its C/O core at explosion.

Key words: supernovae: individual - SN2016coi/ASASSN16-fp.

⋆ E-mail: sipren.astro@gmail.com (SJP); chris.ashall24@gmail.com (CA)

Published by Oxford University Press on behalf of the Royal Astronomical Society

1 INTRODUCTION

In order for the death of a massive star to result in a stripped-envelope supernova (SE-SN) event (Clocchiatti & Wheeler 1997), the progenitor star must undergo a period of severe envelope stripping but how this mass-loss occurs is not fully understood. There are three favoured mechanisms for envelope stripping. The first is through strong stellar winds, which are both metallicity and rotation dependent, and can results in mass-loss rates of 10^{-4}–10^{-5} $M_{\odot}$ yr^{-1} (e.g. Langer 2012; Maeda et al. 2015). However, stellar evolution models of single stars struggle to remove He to the upper limit given by Hachinger et al. (2012) for a He-poor SN.

The second mechanism is episodic mass-loss during a luminous blue variable (LBV) stage, where periodic pulsations eject a few $M_{\odot}$ of stellar material (Smith et al. 2003). This requires a progenitor star of many 10 s $M_{\odot}$ (Foley et al. 2011) and such stars may not lose enough of their H-/He envelopes before core-collapse (Elias-Rosa et al. 2016).

The third is through binary interaction when a star transfers much of its mass to a donor through Roche lobe overflow or the outer envelope is expelled during a common-envelope phase (Podsiadlowski, Joss & Hsu 1992; Nomoto et al. 1994). This third mechanism is the most likely route for all but the most massive progenitors of SE-SNe and allows progenitors of lower mass, which as single stars may explode as SNe IIP, to explode as SE-SN events. This reconciles the discrepancy between the relative rates of core-collapse SNe and mass-driven rates (e.g, Shivvers et al. 2017).

There have been detections of progenitor stars for a few SE-SNe, these are all He-rich (see e.g. Arcavi et al. 2011; Van Dyk et al. 2014; Eldridge et al. 2015; Eldridge & Maund 2016; Kilpatrick et al. 2017; Tartaglia et al. 2017). In the case of SN 1993J (Maund et al. 2004; Fox et al. 2014), SN 2011dh (Folatelli et al. 2014; Maund et al. 2015), and SN 2001ig (Ryder et al. 2018), late time imaging of the explosion site has revealed evidence for companion stars. It is unknown whether these companions would have been close enough to affect the evolution of the SN progenitor. The progenitors of SNe Ic are not well understood. From single star evolution models, they are expected to be Wolf–Rayet stars (e.g. Georgy et al. 2012). However, no confirmed progenitor has yet been seen in archival images placing strict limits on massive WR progenitors (Smartt 2009; Yoon et al. 2012). It has been found that ejecta masses for these He-poor SNe range from $\sim$1 $M_{\odot}$ (Sauer et al. 2006; Mazzali et al. 2010) to $\sim$13 $M_{\odot}$ (Mazzali et al. 2006). This translates into a range of progenitor masses from $\sim$15–50 $M_{\odot}$. The lower end of this distribution is in the range of progenitors of SNe IIP, where observations suggest that $M_{\rm ZAMS}\sim$10–16 $M_{\odot}$ (Smartt 2009; Valenti et al. 2016) and theory predicts progenitors of up to 25 $M_{\odot}$. The discrepancy may be caused by an underestimate in amount of circumstellar extinction (Beasor & Davies 2016).

In this work, we present optical photometric and spectroscopic observations of the nearby SN 2016coi/ASASSN-16fp. The SN is densely sampled between $\sim$20 and 200 d after explosion with 55 spectroscopic observations making SN 2016coi one of the best-sampled SE-SNe to date, a consequence of its early discovery and proximity. This SN was originally classified as a ‘broad-lined’ type Ic SN, but Yamanaka et al. (2017) presented a case for the presence of He in the ejecta. Based upon analytical analysis of the observational data, they proposed a new classification of SN 2016coi as a broad-lined Ib. There have been previous discussions of He in SNe Ic (see e.g. Filippenko et al. 1995; Taubenberger et al. 2006; Modjaz et al. 2014) and some claimed detections [e.g. SN 2012ap (Milisavljevic et al. 2015) and SN 2009bb (Pignata et al. 2011)]. However, none of these claims have provided conclusive proof, indeed, it is possible to infer a detection of He in some SNe Ic from the coincidental alignment of Doppler shifted He lines and absorption features, but these do not behave as He lines do in He-rich SNe. Additionally, there are many more examples where similar features in other SNe Ic are not compatible with He lines. Recent analysis has suggested that SNe Ic with highly blended lines are He free (Modjaz et al. 2016).

The classification of SE-SNe was revisited in Prentice & Mazzali (2017) in order to link the taxonomic scheme with physical parameters. For the SN sample used in that work, it was found that when He was obviously present in the ejecta of an SN it formed strong lines (e.g. there were no examples of weak He lines). This allowed a natural division between He-rich and He-poor SNe. For the He-rich SNe, classification was based upon characterizing the presence and strength of H and led to the subdivision of types Ib and IIb into Ib, Ib(II), IIb(I), and IIb for weakest to strongest H lines in the spectra. For He-poor SNe, classification was based upon line blending and lead to subdivision of the SN Ic category into Ic-$\langle N\rangle$ where $\langle N\rangle$ is the mean number of absorption features in the pre-peak spectra from a set list of line transitions and takes an integer value between 3 and 7. The lower the value of $\langle N\rangle$ the more severe the line blending and a higher specific kinetic energy. Such SNe show high kinetic energies, broad lines, and significant line blending, e.g. SN 1998bw (Iwamoto et al. 1998), SN 1997ef (Mazzali, Iwamoto & Nomoto 2000), SN 2002ap (Mazzali et al. 2002), SN 2003dh (Mazzali et al. 2003), SN 2010ah (Corsi et al. 2011; Mazzali et al. 2013), SN 2016jca (Ashall et al. 2017). The most energetic of these SNe are also associated with gamma-ray bursts (GRBs) (e.g. SN 1998bw/GRB 980425, SN 2003dh/GRB 030329, SN2016jca/GRB 161219B). An injection of $\sim 10^{52}$ erg of energy into the ejecta likely requires some contribution from a rapidly rotating compact object, either a magnetar (Mazzali et al. 2014) or a black hole (Woosley et al. 1994). The maximum rotational energy of these compact objects is a few 10^{53} erg (Metzger et al. 2015) and would have to be injected on a short time-scale in order to influence the SN dynamically but not to influence the light curve.

Some SE-SNe are classified as Ib/c owing to the ambiguity of the presence of He in the spectra (e.g. SN 2013ge, Drout et al. 2016) or lack of spectral coverage. However, a supernova that is genuinely a transitional event between SNe Ic and SNe Ib would be an important discovery and may help to explain why SNe Ic should show no clear indication of He in their spectra and why there is such a sharp distinction between SNe with He and SNe without He. In this work, we use analytical methods and spectral modelling to investigate the physical properties and elemental structure of the ejecta of SN 2016coi.

In Section 2, we detail the observations and data reduction. In Section 3, the host-galaxy of the SN, UGC 11868, is analysed. Sections 4 and 5 present the light curves and associated properties for the multiband photometry and the pseudo-bolometric light curve, respectively. We examine the spectra analytically in Section 6 and model the early spectra and nebular spectra in Section 7. We briefly discuss the SN in Section 8 before presenting our conclusions in Section 9.

2 OBSERVATIONS AND DATA REDUCTION

SN 2016coi/ASASSN-16fp was discovered on 2016-05-27.55 UT by the All Sky Automated Survey for Supernovae (ASAS-SN) (see Shappee et al. 2014) and was located in the galaxy UGC 11868, $z = 0.0036$, at $\alpha = 21^{\rm h}59^{\rm m}04\overset{\rm s}{.}14$ $\delta = +18^{\circ}11'10\overset{''}{.}46$ (J2000) (see

Table 1. Properties of the environment towards the SN.

SN	α (J2000)	δ	Host	z	μ (mag)	$E(B-V)_{\rm MW}$ (mag)	$E(B-V)_{\rm host}$ (mag)
2016coi	21:59:04.14	+18:11:10.46	UGC 11868	0.0036	31.00	0.08	0.125 ± 0.025

Table 1), the last non-detection had been 6 d prior (Holoien et al. 2016). It was subsequently classified as a pre-maximum 'broad lined' type Ic SN on 2016-05-28.52 UT.

Our first observations were taken prior to this on 2016-05-28.20 UT using the Spectrograph for the Rapid Acquisition of Transients (SPRAT; Piascik et al. 2014) on the 2.0 m Liverpool Telescope (LT; Steele et al. 2004), based at the Roque de los Muchachos Observatory. Subsequent photometric and spectroscopic follow-up observations were conducted with by several different facilities around the world:

(i) Photometry and spectroscopy using the optical wide-field camera IO:O and SPRAT on the LT.

(ii) Photometry and spectroscopy via the Spectral cameras and Floyds spectrograph on the Las Cumbres Observatory (LCO) network 2.0 m telescopes at the Haleakala Observatory and the Siding Spring Observatory (SSO), the Sinistro cameras on the LCO 1 m telescopes at the South African Astronomical Observatory (SAAO), the McDonald Observatory, and the Cerro Tololo Inter-American Observatory (CTIO; Brown et al. 2013).

(iii) Photometric and spectroscopic observations from the Li-Jiang 2.4 m telescope (LJT; Fan et al. 2015) at Li-Jiang Observatory of Yunnan Observatories (YNAO) using the Yunnan Faint Object Spectrograph and Camera (YFOSC; Zhang et al. 2014), the Xing-Long 2.16 m telescope (XLT) at Xing-Long Observation of National Astronomical Observatories (NAOC) with Bei-Jing Faint Object Spectrograph and Camera (BFOSC). The spectra of LJT and XLT were reduced using standard IRAF long-slit spectra routines. The flux calibration was done with the standard spectrophotometric flux stars observed at a similar airmass on the same night. Optical photometry were obtained in the Johnson *UBV* and Kron-Cousins *RI* bands by Tsinghua-NAOC 0.8 m telescope (TNT; Wang et al. 2008; Huang et al. 2012); Johnson *BV*, Kron-Cousins *R*, and Sloan Digital Sky Survey (SDSS) *ugriz* bands by LJT with YFOSC.

(iv) Photometry from the 0.6/0.9 m Schmidt telescope, equipped with a liquid-cooled Apogee Alta U16 4096 × 4096 CCD camera (field-of-view 70 × 70 arcmin^2) and Bessell *BVRI* filters, at Piszkéstető Station of Konkoly Observatory, Hungary. The CCD frames were bias-, dark-, and flat-field-corrected by applying standard IRAF routines.

(v) Photometric data from the 0.4 m PROMPT 5 telescope that monitors luminous, nearby (D < 40 Mpc) galaxies (DLT40; Tartaglia et al. in preparation). These data were reduced using aperture photometry on different images (with HOTPANTS; Becker 2015).

(vi) Two spectra using the Kast Double Spectrograph on the Shane 3 m telescope at the Lick Observatory. These were reduced through standard IRAF routines.

(vii) A single spectrum was obtained using the Intermediate Dispersion Spectrograph (IDS), on the 2.5 m Issac Newton Telescope (INT), at the Roque de los Muchachos Observatory in La Palma. The EEV10 detector was used, along with the R400V grating. Data reduction was performed using standard routines within the STARLINK software packages FIGARO and KAPPA, and flux calibrated using custom software.

(viii) A single spectrum from the Deep Imaging Multi-Object Spectrograph (DEIMOS) (Faber et al. 2003) on the W. M. Keck Observatory, Haleakala.

Much of the LCO data, in addition to the Lick spectra, were obtained as part of the LCO Key Supernova Project. For the photometry obtained at Konkoly Observatory, the magnitudes for the SN and some local comparison stars were obtained via PSF-photometry using IRAF/DAOPHOT. The instrumental magnitudes were transformed to the standard system using linear colour terms and zero-points. The zero-points were tied to the PS1-photometry[1] of the local comparison stars after converting their g_p, r_p, i_p magnitudes to BVRI (Tonry et al. 2012). Aperture photometry was performed on the remaining photometric data using a custom script utilizing PYRAF as part of the UREKA[2] package. The instrumental magnitudes were calibrated relative to SDSS stars in the field for the *ugriz* bands. The equations of Jordi, Grebel & Ammon (2006) were used to convert American Association of Variable Star Observers Photometric All-Sky Survey (APASS) standard star *BVgri* photometry into *BVRI* and SDSS *ugriz* photometry into *U*. A series of apertures were used to derive the instrumental magnitudes and the median value taken as the calibrated magnitude. The uncertainty was taken to be either the standard deviation of the photometric equation fit or the standard deviation of the calibrated magnitudes, whichever was larger. SPRAT spectra were reduced and flux calibrated using the LT pipeline (Barnsley, Smith & Steele 2012) and a custom PYTHON script. LCO/Floyds spectra were reduced using the publicly available LCO pipeline.[3]

3 HOST-GALAXY – UGC 11868

3.1 Line-of-sight attenuation

The Galactic extinction in the direction of the SN is $E(B-V)_{\rm MW} = 0.08$ mag (Schlafly & Finkbeiner 2011). $E(B-V)_{\rm host}$ can be calculated through a number of methods including measurement of the equivalent width of the rest-frame Na I D lines (Poznanski, Prochaska & Bloom 2012), and by assessing the colour curve of the SN relative to the bulk of the population where an offset from the mean implies some amount of extinction (e.g. Drout et al. 2011; Stritzinger et al. 2018). Throughout the following methods, it is assumed that $R_V = 3.1$.

We find no indication of strong host Na I D lines in our low-resolution spectra, the Galactic Na I D lines are the dominant component in this regard. The upper limit set by measuring the equivalent width of this weak feature is approximately $E(B-V)_{\rm host} = 0.03$ mag, using the method of Poznanski et al. (2012). It is acknowledged that the low resolution of the spectra may affect the measurement here (Poznanski et al. 2011) and that $E(B-V)_{\rm host}$ may be greater than this, although it could not be significantly larger as experience shows that the host Na I D lines would become prominent in the spectra. In Section 4.1.1, the $g-r$ colour curve of SN 2016coi is examined

---

[1] http://archive.stsci.edu/panstarrs/search.php

[2] http://ssb.stsci.edu/ureka/(deprecated)

[3] https://lco.global/

in relation to other SE-SNe. We find that some small to moderate extinction ∼0.1–0.2 mag in $E(B - V)$ is required to move the colour curve of SN 2016coi into the host-corrected distribution. A correction for $E(B - V)_{\mathrm{host}}$ ∼0.4 mag is required to place the colour curve at the bottom of the distribution. Given the potential for uncertainty we apply a third test. In Section 7, we use spectral models to examine a range of values for $E(B - V)_{\mathrm{host}}$ and determine that it could be anywhere from $E(B - V)_{\mathrm{host}} = 0.1$–0.15 mag. Considering the results from the different methods here, we adopt a $E(B - V)_{\mathrm{host}}$ of 0.125 ± 0.025 mag, and an $E(B - V)_{\mathrm{tot}} = 0.205 \pm 0.025$ mag. The upper limit is constrained by the weakness of the host Na I D absorption lines in the spectra.

3.2 The properties of UGC 11868

The host galaxy of SN 2016coi is UGC 11868, also known as II Zw 158 and MCG +03-56-001. The distance to UGC 11868 is somewhat uncertain (see NASA/IPAC Extragalactic Database[4] for more details), and in this work, we adopt a distance modulus of 31.00 mag. This value is taken as absolute with no uncertainty included in order to enable easy conversion of the intrinsic light-curve properties, including uncertainties derived from the photometry and reddening, for different distances.

UGC 11868 is a low-surface-brightness, low-luminosity galaxy of quite irregular morphology, classified as SBm in the RC3 (de Vaucouleurs et al. 1991). UGC 11868 was included in the H α Galaxy Survey (James et al. 2004) which included R band and narrow-band H α imaging (See Figures 1 and 2). Correcting the data from that study to an adopted distance of 15.8 Mpc, distance modulus 31.00, UGC 11868 has an apparent R-band magnitude of 13.10, an absolute R-band magnitude of −17.90, and a star formation rate of 0.078 $\mathrm{M}_{\odot}\,\mathrm{yr}^{-1}$. The latter value has been corrected for internal extinction using the absolute-magnitude-dependent extinction formula of Helmboldt et al. (2004), since the global correction of 1.1 mag applied by James et al. (2004) is almost certainly an overestimate for such a low-luminosity system. The Magellanic Clouds provide useful reference points for UGC 11868, with star formation rates of 0.054 and 0.23 $\mathrm{M}_{\odot}\,\mathrm{yr}^{-1}$, and absolute R-band magnitudes of −17.10 and −18.50 for the SMC and LMC, respectively. The $\mu_B = 25$ isophotal diameter from RC3 corresponds to 9.0 kpc for our adopted distance, similar to the 9.5 kpc value for the LMC, which also shares its SBm classification with UGC 11868. Thus, host of SN2016coi is very similar to the LMC overall, but slightly more diffuse and lower in surface brightness. The somewhat higher star formation rate for the LMC can be entirely attributed to the unusually powerful 30 Doradus complex; the star formation properties of UGC 11868 appear entirely normal for its type.

SN 2016coi lies well away from the centre of UGC 11868. There is no well-defined nucleus, just a somewhat elongated general region of higher surface brightness that gives rise to the barred classification. Defining the highest surface brightness region from the R-band image as the galaxy centre, we determine that SN 2016coi occurred 34 arcsec or 2.6 kpc from this location. There is no detectable H α emission at the location of the SN; a moderately bright region is located 5 arcsec or 375 pc away.

There are no direct metallicity measurements for UGC 11868, but again the comparison with the Magellanic Clouds and other dwarf galaxies can be used to give some indications of likely values. Berg et al. (2012) calibrate a correlation between absolute magnitude and oxygen abundance for star-forming dwarf galaxies, from which we derive a value of 12+log(O/H) = 8.21, very close to the measured value of 8.26 for the LMC from the same study. In terms of [Fe/H], Cioni (2009) show a central value of ∼−1.0 for the LMC, but this falls to −1.3 in the outer regions, matching the global value derived for SMC which has no detectable radial gradient. Thus, inferred values of 12+log(O/H) = 8.21, [Fe/H] = −1.3 are plausible estimates for the location of SN 2016coi.

To conclude, SN 2016coi occurred in the outer regions of a low-luminosity, LMC-like host galaxy, in a location with almost certainly low metallicity and nearby but not coincident ongoing star formation. The sub-solar metallicity is consistent with studies of the local environments of non-GRB 'broad-lined' SNe Ic (see Modjaz et al. 2008, 2011; Sanders et al. 2012).

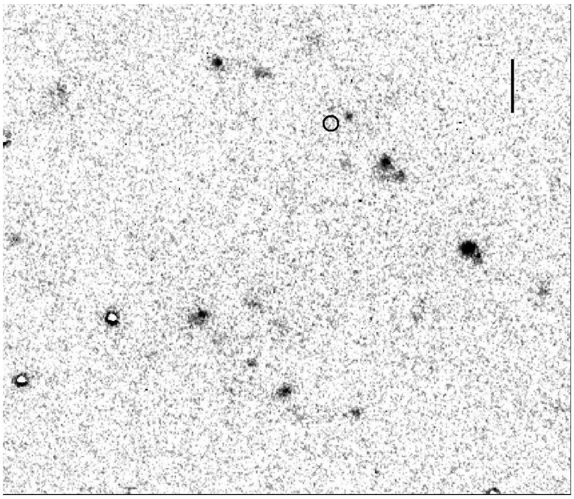

Figure 1. A pre-explosion H α image of UGC 11868. The position of SN 2016coi is designated by the circle. There is no strong emission at the location of the SN, suggesting a region of little star formation. North is up and East is left. The scale bars, located in the upper right corner of the image, corresponds to 13.0 arcsec, or 1 kpc at the adopted distance of 15.85 Mpc, $\mu = 31.0$ mag.

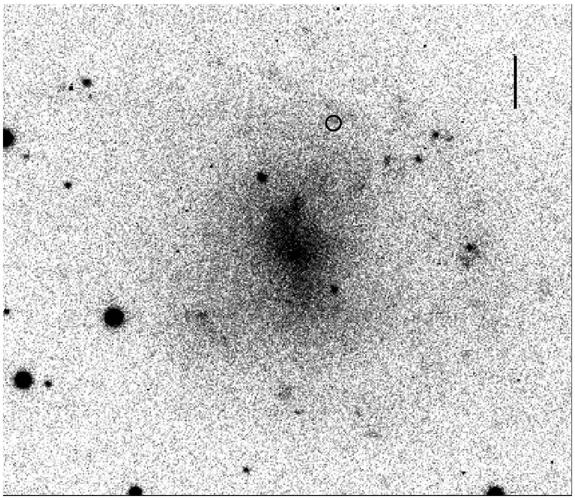

Figure 2. A pre-explosion r-band image of UCG 11868 taken on 2000 July 6. The position of the SN is shown by the circle. See Fig. 1 for orientation and scale.

---

[4] http://ned.ipac.caltech.edu/

4 LIGHT CURVES

Fig. 3 shows the *ugriz* (Table D2), *UBVRI* (Table D3), and DLT40 Open*r* (Table D4) light curves of SN 2016coi; these are not corrected for extinction but are presented in rest-frame time.

We fit the extinction corrected light curves to find the peak magnitude $M_{\rm peak}$, and three characteristic time-scales. These are $t_{-1/2}$, $t_{+1/2}$, and the late linear decay rate $\Delta m_{\rm late}$. $t_{-1/2}$ and $t_{+1/2}$ measure the time taken for the light curve to evolve between the maximum luminosity $L_{\rm p}$ and $L_{\rm p}/2$ on the rise and decline, respectively.

Light-curve parameters were measured by fitting a low-order spline from UNIVARIATESPLINE as part of the SCIPY package. Errors were estimated to be within the confines of the uncertainty in the photometry and the order of the spline was allowed to vary to estimate the effect on the fit. We find that variations in the spline fit produced either a negligible effect or were clearly wrong. For M the errors are small and dominated by the uncertainty in $E(B-V)_{\rm tot}$.

The time for the light curve to rise from explosion to peak $t_{\rm p}$ is, with the exception of GRB-SNe where the detection of the high-energy transient signals the moment of core collapse, an unknown quantity. Comparatively, $t_{-1/2}$ is a measurable quantity for many SNe so allows for comparison. $t_{\rm p}$, and by proxy $t_{-1/2}$, is affected by the ejecta mass $M_{\rm ej}$ the ejecta velocity, and the distribution of ^{56}Ni within the ejecta (e.g. Arnett 1982). Mass increases the photon diffusion time, while the ejecta velocity decreases it. Placing small amounts of ^{56}Ni in the outer ejecta causes the light curve to rise quicker as the photons are able to diffuse through the low-density, high-velocity, outer ejecta more rapidly. The post peak decay time is more affected by the core mass as the outer layers are now optically thin. The late decay follows a linear decline which is the result of energy injection from the decay of ^{56}Co to ^{56}Fe and is affected by the efficiency of the ejecta to trap γ-rays and positrons. In the vast majority of SE-SNe, the late decay rate exceeds that of ^{56}Co, implying that the ejecta are not 100 per cent efficient at trapping gamma rays.

Table 2 gives the properties of the multiband light curves, corrected for $E(B-V)_{\rm tot}$ using the reddening law of Cardelli, Clayton & Mathis (1989). As is typical of SE-SNe the redder bands evolve more slowly (see Drout et al. 2011; Bianco et al. 2014; Taddia et al. 2015, 2018) with values ranging between ~8 and 14 d. It is noticeable that the light curves are more asymmetric for the redder bands. The late-time decay rates are in the range of 0.015–0.023 mag d^{-1}.

4.1 Colours

In Fig. 4, we present the colour curves of $g-r$, $g-i$, $r-i$, $B-V$, $V-R$, and $R-I$. The behaviour of the curves shows many features that are typical to SE-SNe. In all colours, there is an initial blueward evolution, as the energy deposited from the decay of ^{56}Ni into the ejecta exceeds radiative losses and the photosphere recedes towards the heat source, so the SN gets bluer and more luminous (Hoeflich et al. 2017). Around the time when $E_{\rm out} > E_{\rm in}$, the SN ejecta expands adiabatically, cooling the photosphere, which leads to a decrease in luminosity. The cooling photosphere results in a redward turn in the colour curves. After ~+20 d, $g-r$ and $g-i$ turn blue again as the flux in the red decreases due to the loss of the photosphere. At ~+ 100 d, the SN is in the early nebular phase, and in $g-r$ and $g-i$, there is then a turn back towards the red. This is driven by the appearance of the [O I]λλ6300, 6364 emission line which dominates the flux in the *r* band and the Ca II] λλ7291, 7324, O I λ7773, and [S I λ7722 emission lines which dominate the flux in the *i* band. Comparatively, there are few strong emission lines around the effective wavelength of *g* (~4770 Å), the strongest emission feature being a blend of Mg I] λ4570 and [S I] λ4589.

$r-i$ slowly evolves to the blue from about ~+50 d as the emission line flux in *r* is greater than that in *i*. Without the dramatic change in flux seen in *g*, the curve does not show a late blue turn during the time of our observations.

4.1.1 *Comparison of* g − r *with He-poor SNe*

The $g-r$ colour curve of SN 2016coi is shown in relation to He-poor SNe in Fig. 5. The application of an extinction correction $E(B-V)_{\rm MW} = 0.08$ mag places the colour curve at the upper edge of the distribution. To place the curve in the middle of the distribution requires a host-extinction of $E(B-V)_{\rm host}$ ~0.25 mag, which is incompatible with the weak the host Na I D lines. A moderate correction of $E(B-V)_{\rm host}$= 0.05–0.15 places the SN at the upper edge of the distribution. The figure is shown with our total $E(B-V)_{\rm tot} = 0.205 \pm 0.025$ mag applied. This suggests that the SN is intrinsically red.

5 BOLOMETRIC LIGHT CURVE

The pseudo-bolometric light curve (henceforth 'bolometric') was constructed using the de-reddened *griz* photometry converted to monochromatic flux (Fukugita et al. 1996). The resulting spectral energy distribution (SED) was integrated over the range of 4000–10 000 Å and then converted to luminosity using $\mu = 31.00$ mag. The bolometric light curve is presented in comparison with He-poor SE-SNe in Fig. 6. The *u*-band data were not included at this point as the 4000–10 000 Å range allows direct comparison of the pseudo-bolometric light curve properties of a large number of SE-SNe. However, in Table 3 we present the statistics obtained from the pseudo-bolometric light curve using the *u*-band data (integrating over 3000–10 000 Å), and estimating the fully bolometric $L_{\rm p}$ as per the method given Prentice et al. (2016). This latter method utilizes a relation between the *ugriz* integrated light curves of various SE-SNe and their *ugriz* plus near-infrared (NIR) 10 000–24 000 Å light curves in order to estimate the missing NIR flux. This value is then increased by 10 per cent to account for flux outside the wavelength regime to give an estimate of the UVOIR $L_{\rm p}$.

SN 2016coi reached a peak luminosity (*griz*) of $\log_{10}(L_{\rm p}/{\rm erg\,s^{-1}}) = 42.29 \pm 0.02$ or, alternatively, $L_{\rm p} = (1.9 \pm 0.1) \times 10^{42}$ erg s^{-1}. The temporal values, calculated by fitting a low order spline to the light curve, were found to be $t_{-1/2} = 12.4 \pm 0.5$ d and $t_{+1/2}$= 23 ± 1 d, which equates to a width of 35 ± 1 d. Extrapolation from a simple quadratic fit to the pre-peak light curve reveals that the progenitor exploded approximately 2 ± 1 d before discovery of the SN, which is consistent with the explosion date found from spectral modelling (see Section 7). For this light curve, the time from rise to peak $t_{\rm p}$ = 17 ± 1 d. The late time decay rate is calculated by fitting a linear function to the decline; this returns a decay rate of ~0.015 mag d^{-1}.

When including the *u* band, the peak luminosity increases by 23 per cent to $L_{\rm p} = (2.4 \pm 0.1) \times 10^{42}$ erg s^{-1}. Inclusion of the *u* band makes the light curve rise and decay slightly quicker ($t_{-1/2} = 11 \pm 1$ d, $t_{+1/2} = 19 \pm 2$ d), as would be expected from the increased energy at early times. It is calculated that the time from explosion to $L_{\rm p}$, $t_{\rm p}$= $16\pm^{1.3}_{0.7}$ d, which includes an estimated ~1 d of 'dark time' (Corsi et al. 2012).

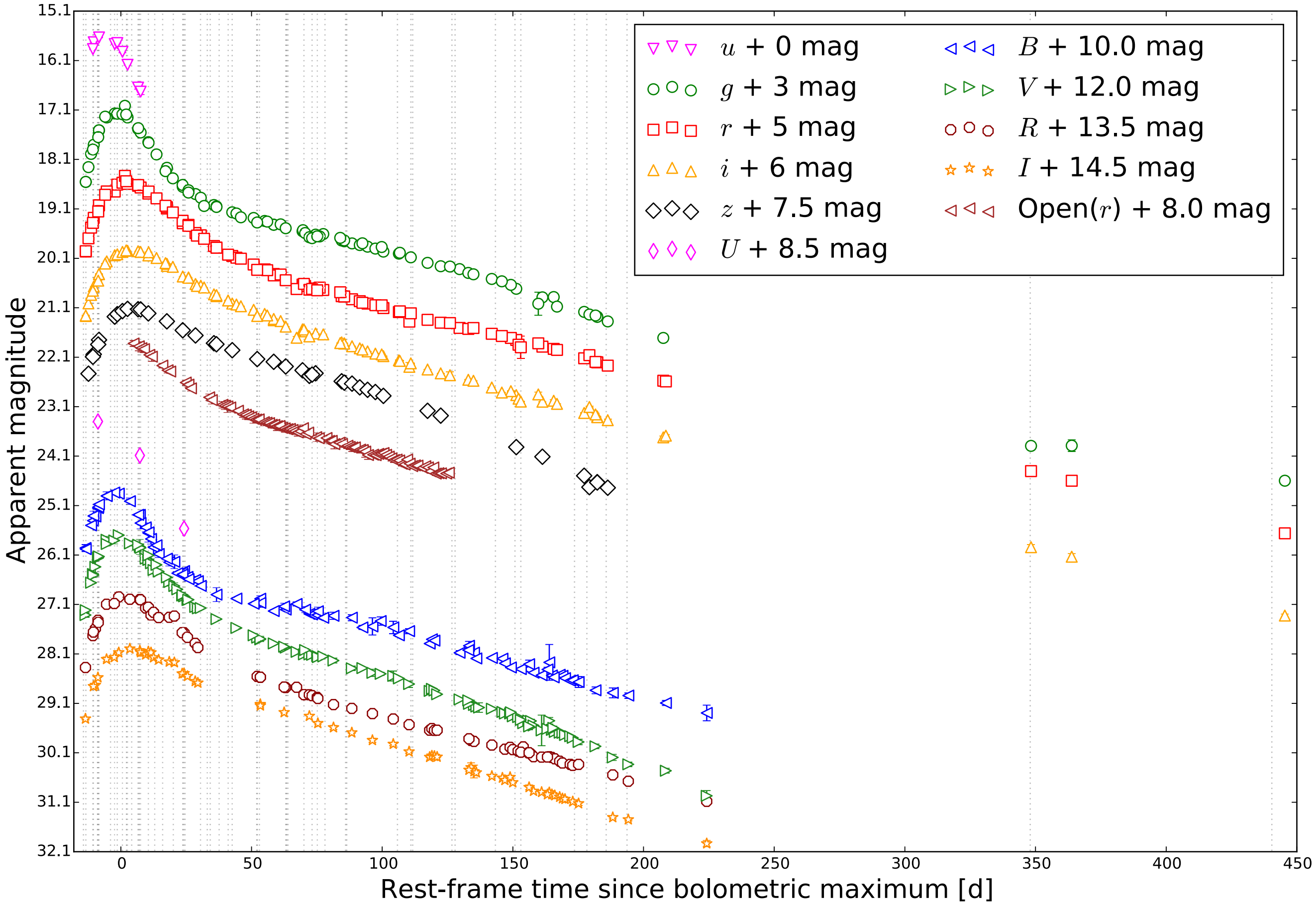

Figure 3. The LT, LCO, TNT, LJT, Konkoly, and DLT40 *ugriz*, *UBVRI*, and Open(r) light curves of SN 2016coi shifted to rest-frame time. This period covers from shortly after explosion to the nebular phase. The grey dotted lines represent dates of spectroscopic observations.

Table 2. Multiband light-curve properties.

Band	$M_{\rm peak}$ (mag)	$t_{-1/2}$ (d)	$t_{+1/2}$ (d)	$\Delta m_{\rm late}$ (mag d^{-1})
u	− 16.4 ± 0.1	–	11 ± 0.5	–
g	− 17.61 ± 0.09	8.7 ± 0.1	13.3 ± 0.5	0.015
r	− 17.97 ± 0.07	11.8 ± 0.1	21.0 ± 0.5	0.014
i	− 17.46 ± 0.06	13.1 ± 0.1	28.4 ± 0.5	0.016
z	− 17.66 ± 0.04	13.2 ± 0.5	34 ± 1	0.019
B	− 18.3 ± 0.1	9.6 ± 0.5	12.5 ± 0.5	0.014
V	− 17.93 ± 0.07	10.3 ± 0.5	14.4 ± 0.4	0.016
R	− 18.10 ± 0.06	12.3 ± 0.5	20.1 ± 0.5	0.013
I	− 17.9 ± 0.05	13.7 ± 0.5	26.5 ± 0.7	0.016

Finally, the estimated UVOIR bolometric luminosity is $\sim 3 \times 10^{42}$ erg s^{-1}. This is commensurate with that found through spectral modelling (see Section 7).

5.1 Estimating $M_{\rm Ni}$

To estimate the amount of ^{56}Ni synthesized during explosive silicon burning in the first few seconds following core collapse we utilize the following equation from Stritzinger & Leibundgut (2005)

$$\frac{M_{\rm Ni}}{{\rm M}_\odot} = L_{\rm p} \times \left(10^{43}{\rm erg~s^{-1}}\right)^{-1} \times \left(6.45 \times {\rm e}^{-tp/8.8} + 1.45 \times {\rm e}^{-tp/111.3}\right)^{-1} \qquad (1)$$

which is based upon the formulation for $M_{\rm Ni}$ given in Arnett (1982) and assumes that the luminosity of the SN at peak is approximately equal to the energy emitted by the decay-chain of ^{56}Ni at that time. Using a rise time from explosion to peak of $t_{\rm p}$ 17 d and 16 d, for the *griz* bolometric and *ugriz* bolometric $L_{\rm p}$, respectively, we find that $M_{{\rm Ni},griz} = 0.09 \pm 0.01\,{\rm M}_\odot$ and $M_{{\rm Ni},ugriz} = 0.104^{0.02}_{0.008}\,{\rm M}_\odot$. The nickel mass derived from the estimated fully bolometric luminosity corresponds to $M_{\rm Ni,UVOIR} \sim 0.14\,{\rm M}_\odot$. These values are based on the assumption that all the ^{56}Ni is located centrally. In reality, there will be some distribution of ^{56}Ni throughout the ejecta, which causes the light curve to rise faster than in the centrally located case, and some degree of asphericity (Maeda et al. 2008; Stevance et al. 2017). The result is that a lower $M_{\rm Ni}$ can achieve the same results.

5.2 Comparison of bolometric properties with SNe Ic

Table 3 gives the properties of SN 2016coi derived from the *griz* and *ugriz* light curves. SN 2016coi is quite typical in luminosity (4000–10 000 Å) compared to He-poor SNe where the mean for

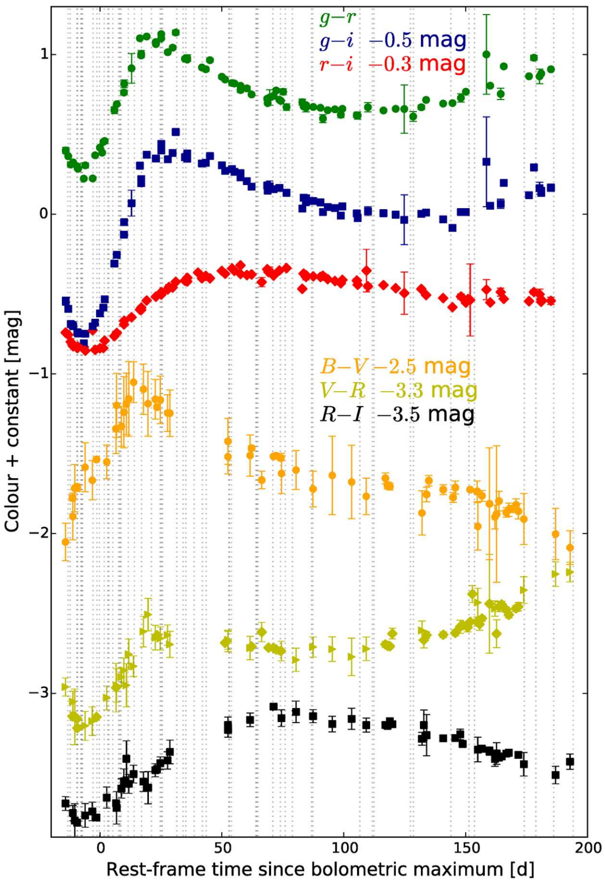

Figure 4. The colour evolution of $g-r$, $g-i$, $r-i$, $B-V$, $V-R$, and $R-I$ to +200 d. The photometry is corrected for $E(B-V)_{\rm tot}$ and is presented in the rest frame. The dotted lines represent spectroscopic observations.

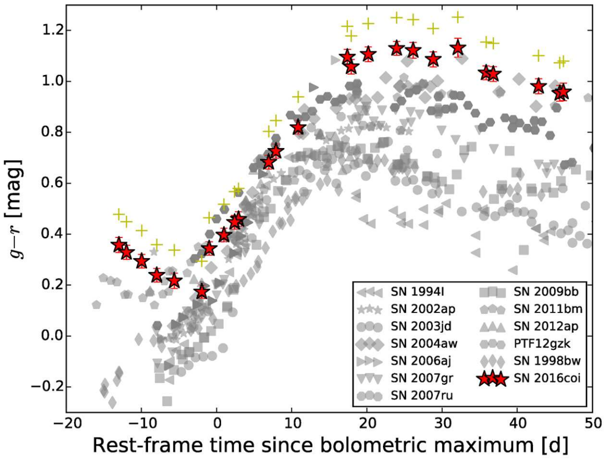

Figure 5. The $g-r$ colour evolution of SN 2016coi in relation to other SNe Ic from the sample of Prentice et al. (2016). The photometry has been corrected for $E(B-V)_{\rm tot}$ and our errors have been included on the plot so as to show the possible movement of the colour curve in relation to the distribution. In the absence of $E(B-V)_{\rm host}$ (yellow), the colour curve sits on the very top of the distribution. Our analysis suggests that 2016coi is intrinsically red.

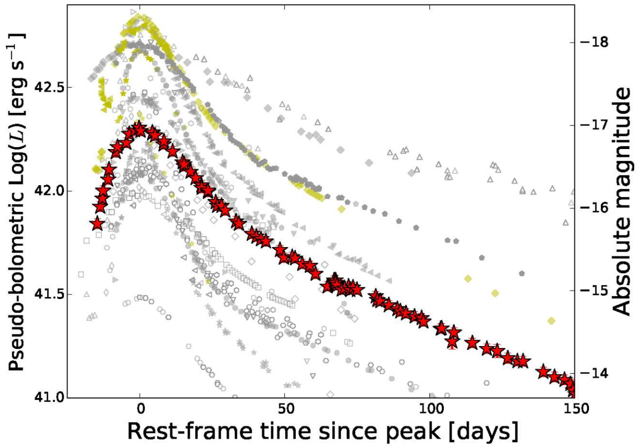

Figure 6. The *griz* optical pseudo-bolometric light curve of SN 2016coi (red) set in context against SNe Ic (Prentice et al. 2016). The open symbols represent SNe with no correction for host extinction applied, GRB-SNe are shown in yellow. SN 2016coi is not extreme in either luminosity or temporal evolution.

non GRB-SNe is $\log_{10}(L_{\rm p}/{\rm erg\,s^{-1}}) = 42.4 \pm 0.2$. Fig. 6 plots the *griz* light curves of SN 2016coi and SNe Ic.

The mean $t_{-1/2}$ and $t_{+1/2}$ of SNe Ic are 10 ± 3 d and 20 ± 9 d, respectively, while the mean width for those SNe where it can be calculated is 30 ± 11 d. The values derived for SN 2016coi suggest it to be above average but within one sigma of the mean. Fig. 7 plots $t_{-1/2}$ against $t_{+1/2}$ and demonstrates that SN 2016coi is on the upper end of the $t_{-1/2}$ and $t_{+1/2}$ distribution. It is not, however, akin to SNe Ic with very broad light curves (e.g. SN 1997ef Mazzali et al. 2000). SN 2016coi is long in both rise and decay compared to the mean and median values of both parameters for the population; however, the mean values are skewed to longer durations by the slowly evolving SNe. $M_{\rm ej}$ is considered in Section 7 but the results here suggest that $M_{\rm ej}$ of SN 2016coi is larger than average for He-poor SNe.

Fig. 8 shows the distribution of $M_{\rm Ni}$ constructed from the 4000–10 000 Å pseudo-bolometric light curves. Not all of the SNe have been reclassified under the scheme given in (Prentice & Mazzali 2017), thus we group 'normal SNe Ic' with Ic-5, 6, & 7, and 'Ic-BL' with Ic-3 and Ic-4. We do not include GRB-SNe in this plot. The median $M_{\rm Ni}$ is $0.09^{+0.08}_{-0.03}$ M$_{\odot}$ for all the SNe. In considering just the Ic-3/4 (broad-line) group, to which SN 2016coi belongs, we find the median $M_{\rm Ni} = 0.10^{+0.07}_{-0.03}$ M$_{\odot}$. The distribution is clearly skewed, driven by a few luminous and long-rising SNe. Both measures suggest that $M_{\rm Ni}$ for SN 2016coi is consistent with the bulk of the population.

6 SPECTROSCOPY

Our spectroscopic coverage of SN 2016coi is dense, with 55 spectra in total. These are presented as a select time series in Fig. 9 and fully in Figs C1 –C4 in Appendix C. Our spectral observations average one spectrum every 2 d until 2 months after the date of classification. The spectral sequence here is sufficiently dense to follow the evolution of features between 4000 and 8000 Å during the photospheric phase in detail, when the SN is defined by absorption features rather than emission lines. Late time spectroscopy follows the SN from the photospheric phase and extends into the early nebular phase. The first indication of transition into the nebular phase is seen at around ∼+63 d, shown in Fig. 9, as the [O I]λλ 6300, 6363 emission line is clear to see around 6300 Å. It is absent

Table 3. Statistics derived from the pseudo-bolometric light curves.

Bol. type	$\log_{10}(L_p/\mathrm{erg\,s^{-1}})$	$t_{-1/2}$ (d)	$t_{+1/2}$ (d)	Width (d)	$t_{\max}$ (d)	Δm_{late} (mag d^{-1})	M_{Ni} M$_\odot$
griz	42.29 ± 0.02	13 ± 1	23 ± 1	36 ± 2	17 ± 1	0.015	0.09 ± 0.01
ugriz	42.38 ± 0.01	11 ± 1	19 ± 2	32 ± 2	$16\pm^{1.3}_{0.7}$	–	$0.104\pm^{0.02}_{0.008}$
UVOIR∗	∼42.51	–	–	–	–	–	∼0.14

∗Estimated – see the text.

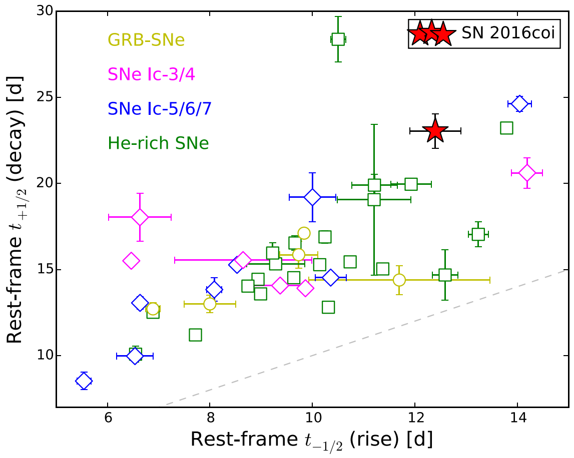

Figure 7. $t_{-1/2}$ against $t_{+1/2}$, as calculated from the 4000–10 000 Å light curve, for SE-SNe where the SN has a measurement of both values (Prentice et al. 2016). SN 2016coi is outside the bulk of the population in both properties, but it is still within one sigma of the mean. The most extreme SNe Ic, those with long rise and decay times, are outside the field of view of this plot.

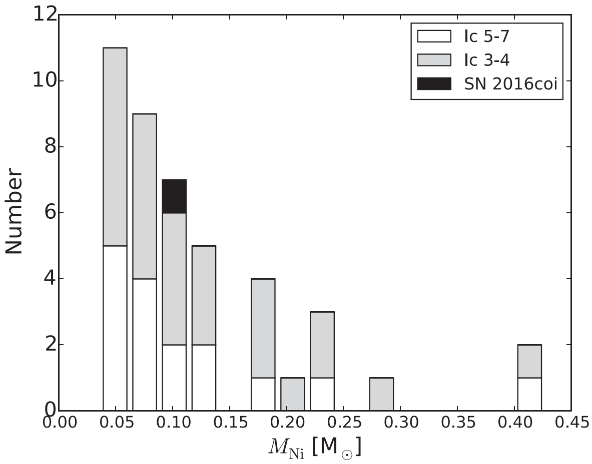

Figure 8. The nickel mass distribution as derived from the 4000 to 10000 Å pseudo-bolometric light curves for He-poor SNe (Prentice et al. 2016). To maximize the sample, we have included SNe that have not been reclassified under the scheme given in Prentice & Mazzali (2017) and assigned 'Ic-BL' SNe to the Ic-3/4 distribution and all other SNe Ic to the Ic-5/6/7 group. SN 2016coi is at the median M_{Ni} for all the SNe and is below, but within one sigma, of the median for Ic-3/4 SNe.

in the spectrum 10 d previous. This line continues to become more prominent against the fading continuum flux for the next month. Comparison with the colour evolution of $g - r$ in Fig. 4 shows that as this feature gets stronger the colour curve turns from blue to red, the reversal of the blueward evolution occurs on day +110 and it is around this time that the SN can be considered to be in the nebular phase as emission lines dominate the flux.

The journal of spectroscopic observations is presented in Table D1. We also discuss the presence of some static features in the pre-peak spectra in Appendix A.

6.1 Preliminary classification

SN 2016coi was originally classified as a broad-line SN Ic. Indeed, it has many spectroscopic similarities to Ic-3/4 SNe. In Fig. 10, we show SN 2016coi in conjunction with Ic-4 SN 2002ap (Mazzali et al. 2002) and SN Ib(II) 2008D (Mazzali et al. 2008; Modjaz et al. 2009), the spectral epochs are scaled as close to SN 2016coi according to relative light-curve width wherever possible. SN 2002ap is a typical He-poor SN with broad spectral features. SN 2008D, associated with X-ray flash 080109, showed broad lines in its early spectra and was originally classified as a SN Ic. However, He lines gradually appeared confirming its classification as a He-rich SN.

The supernovae are similar in the early spectra, all showing broad absorption features. However, there are differences in velocity and strength of these features. In the case of SN 2008D (∼12 d before $t_{\max}$), the first signs of broad He can be seen around ∼5600 and ∼6400 Å. SN 2016coi (∼13 d before $t_{\max}$) shows more features than the SN 2002ap (∼3 9 d before $t_{\max}$) but fewer than SN 2008D. In each case the O I λλ 7771, 7774, 7775 and Ca II NIR triplet remain blended. As the SNe move towards peak SN 2016coi retains a similar spectral shape to SN 2002ap, but with stronger features and a prominent ∼5500 Å absorption. In SN 2008D, the lines become narrower and more prominent. Shortly after peak SN 2002ap and SN 2016coi show many of the same features with the key difference being the strength and velocity of these features. SN 2008D has progressed to look more like a standard He-rich SN. The later spectra demonstrate that there is a tendency to spectral similarity for He-rich and He-poor SNe.

If we consider the similarity of SN 2016coi and SN 2002ap at peak then, from the classification scheme in Prentice & Mazzali (2017), typical Ic-4 SNe show three blended lines at $t_{-1/2}$ and 5 at $t_{\max}$. SN 2016coi is a little different in this regard in that it fulfils the criteria for 4 lines at $t_{-1/2}$ and 4 lines at $t_{+1/2}$, as shown in Fig. 11. Clearly the earliest spectra are different as SN 2016coi shows more structure in its spectra that SN 2002ap, the most obvious difference is the appearance and strength of the absorption features around 5500 and 6000 Å. In SNe Ic, the features are normally attributed to Na I D and Si II λ 6355, respectively, but in light of the comparison here, and the findings of Yamanaka et al. (2017), could it be that Helium contributes to, or is entirely responsible for, the former? In Section 7 this possibility is investigated using a spectrum synthesis code, here were consider more analytical methods.

6.1.1 Testing for He via line profile

Fig. 12 demonstrates a test for common line forming regions using spectra in velocity space. Three prominent helium lines are

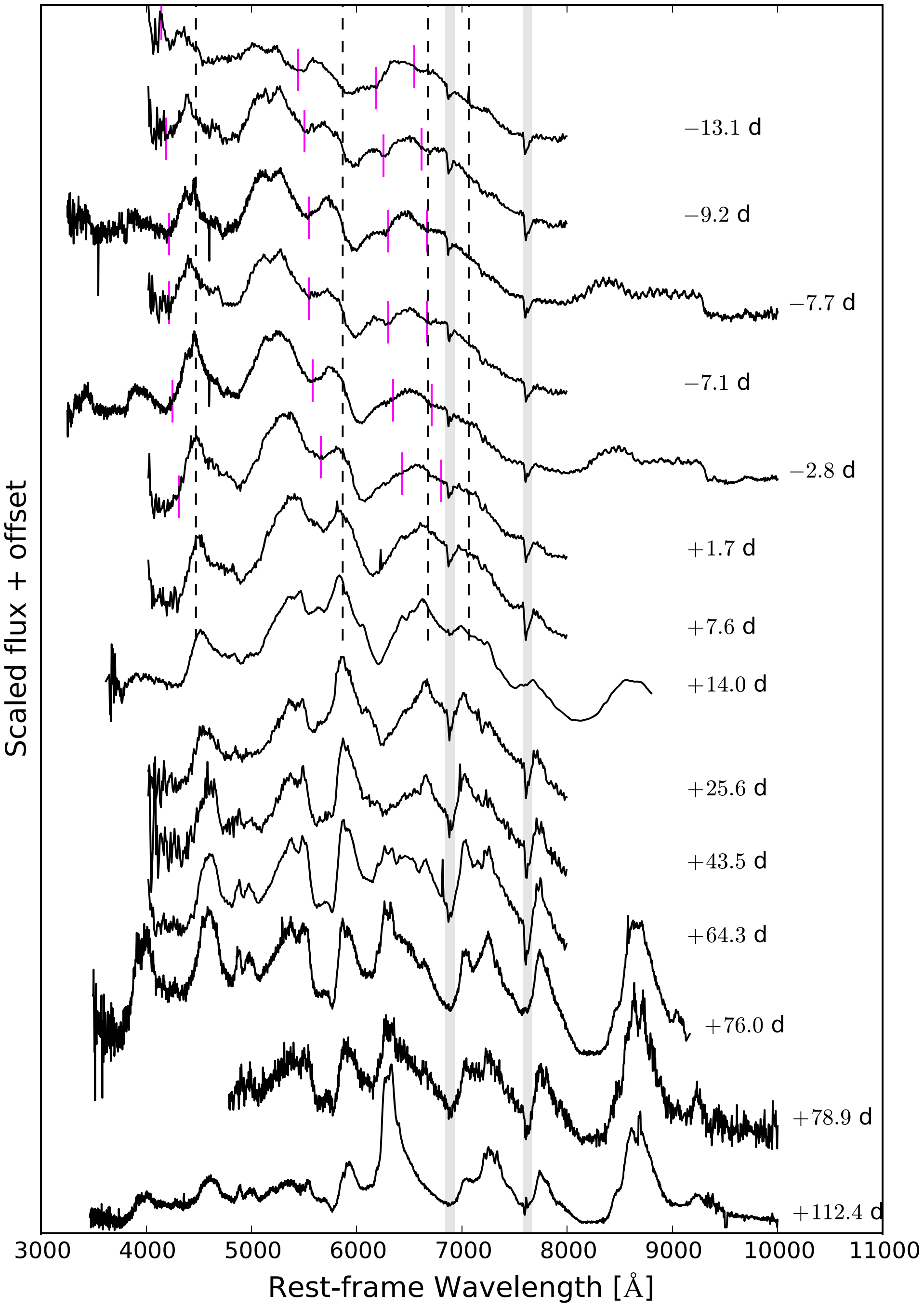

Figure 9. A select time series of spectra of SN 2016coi showing progression from ∼2 d after explosion until the nebular phase. Labelled versions of the spectra can be found in Section 7. The light grey regions identify strong telluric features, the black dashed lines the rest wavelengths of He I λλ4472, 5876, 6678, 7065, and magenta the Doppler shifted position of these lines as given by the velocity from He I λ5876 and the minimum of the blueward absorption profile.

plotted on top of each other at four separate epochs. If the shape of the absorption profiles and the absorption minima (i.e. the velocities) are the same then the lines are formed in the same region, which is evidence for line transitions from the same element.

In the case of He-rich SN 2016jdw, the line profiles are very similar (see the top panel of Fig. 12), indicating that the line-forming regions are the same and a result of absorption by He. However, with SN 2016coi the absorption profiles are dissimilar in both shape and absorption minima. The closest similarity is at −9.2 d. The presence of broad lines complicates matters here as, aside from the width of the lines, multiple species occupy the same line-forming region making it difficult to attribute the feature to one dominant transition. Thus, the identification of He cannot be confirmed as for the most part the absorption profiles are not similar at these epochs.

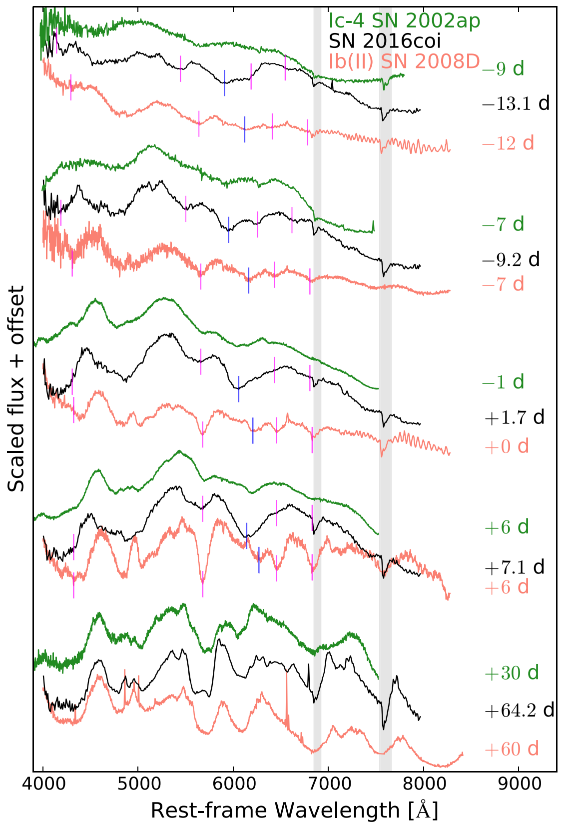

Figure 10. The spectra of SN 2016coi (black) in comparison with Ic-4 SN 2002ap (green) and He-rich SN 2008D (red) at various epochs. Magenta/blue lines show the position of Doppler shifted He I and Si II lines. The evolution of SN 2016coi is slower than that of SN 2002ap, which is to be expected as the time-scales are longer for SN 2016coi. It is noticeable that SN 2016coi has more features visible in the early spectra, especially with respect to the Na I D line at ∼5500 Å. It can also be seen that the SN 2016coi line velocities are lower than SN 2002ap at very early times but are higher by peak. SN 2008D initially has broad lines that give way to a spectrum with strong narrow lines and dominated by He at peak.

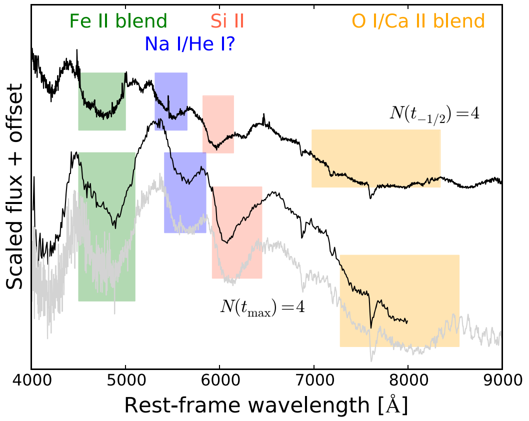

Figure 11. The classification spectra of SN 2016coi at $t_{-1/2}$ (top) and $t_{\max}$ (bottom). The light grey spectrum is at +2.6 d and is included to show the blending of the O I and Ca II lines around 7500–8000 Å. Highlighted are the line blends used to determine N, and consequently $\langle N \rangle$. The SN has $N=4$ at both epochs which leads to the classification of a Ic-4 SN, but matters are complicated if He is present in the ejecta as it would no longer fit into this classification scheme.

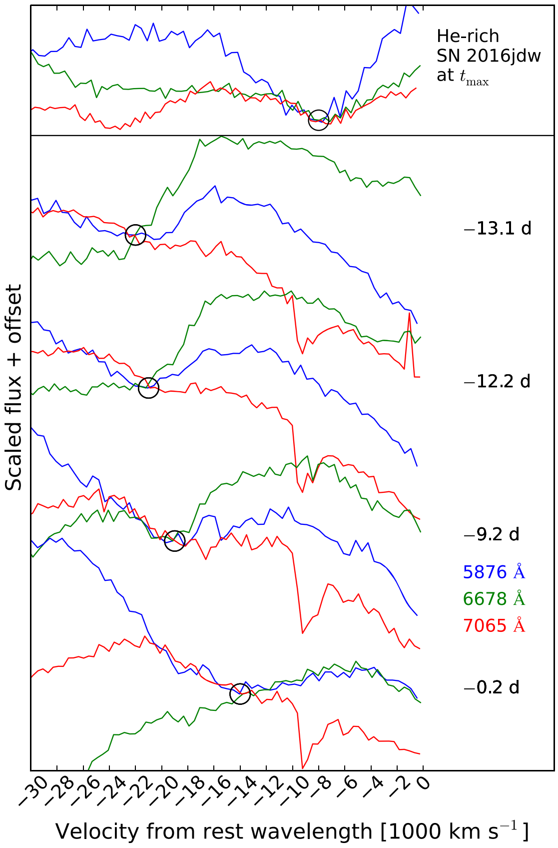

Figure 12. In order to test line profiles for a common origin, we plot the pre-peak spectra of SN 2016coi, in velocity space relative to the rest wavelength of the He λ 5876 (blue), λ 6678 (green), and λ 7065 (red) lines. The flux at a common velocity, as determined by the velocity measured from the 5876 Å, relative to the rest wavelength is used to normalize each spectral region. For comparison the maximum light spectrum of the He-rich SN 2016jdw is included, which demonstrates how He forms within a common line-forming region. In SN 2016coi, the 5876 Å line profile occasionally matches the shape of one of the other two in either the red or the blue, but at no point do the absorption features well match each other.

6.2 Photospheric phase

The first spectrum is taken at −13.1 d (Fig. 9), approximately 2 d after explosion. It is defined by several prominent absorption features. In Section 7, we apply spectroscopic modelling to investigate these features further. In SN 2016coi, these lines, while broad, also appear well defined. This is unusual, as 'broad-lined' SNe typically have fewer than 4 lines visible at this epoch (See Fig. 10). The blue-most absorption features at ∼5000 Å are normally attributed to blends of Fe II lines, while in the middle of the spectrum the two features at ∼5500 and ∼6000 Å are usually attributed to blends of Na I D and He I λ 5876, and Si II λ 6355 and H α, respectively, in He-rich SNe and just Na I D and Si II λ 6355 in He-poor SNe. 7000–8000 Å is dominated by a blend of O I λλ 7771, 7774, 7775 and the Ca II NIR triplet. In the blue, the Fe II group around 5000 Å appears to remain blended until a week after maximum, when there are weak indications of the three prominent Fe II lines (λλ 4924, 5018, 5169). This behaviour is common in broad-lined SNe. Evolution of the 5500 and 6000 Å features (Fig. 9) indicates that both are constructed of several components. The 5500 Å feature appears to be formed from at least two components of similar strength. At

Table 4. Lines used to define velocity.

Ion	λ/(Å)
Fe II	4924
Fe II	5018
Fe II	5169
He I	5876
Na I	5891
Si II	6355
O I	7774
Ca II	NIR triplet

around 0 to +7 d (Fig. 9), the red component briefly becomes the stronger of the two after which the blue component dominates. At no point do these lines fully de-blend. The ∼6000 Å line de-blends into what is normally considered to be SiII λ6355 and C II λ 6580 Å, the latter of which could be He I λ6678. The 6000 Å feature remains very strong and well defined until ∼3 weeks after maximum. The emission peak immediately blueward, associated with NaI D, becomes sharp from ∼ +7 d and can be traced all the way to the nebular phase. The OI and Ca II NIR blend remains in place until ∼ +6 d, at which point the OI absorption becomes distinct.

6.2.1 *Line velocities*

We calculate the line velocities for various features, which we attribute to the lines given in Table 4. It is important to note however that our labelling is not meant to be a conclusive line identification (see Section 7) and that some features are blends of several lines. This is especially important with the Fe II region around 5000 Å where the Fe II λλ4924, 5018, 5169 lines blend with each other and with other lines in the region.

Measurements are taken from the minimum of the absorption feature. The uncertainty on this value is then the range of velocities in that region that returns a similar flux to that of the minimum. For example, a narrow line will result in a small range of velocities as the flux rises rapidly around the minimum. For broader lines the absorption is shallower, resulting in a larger range of possible velocities. Thus, the uncertainty is related to the degree of line blending. Also, in highly blended lines it is extremely unlikely that the measured minimum is caused by a single line (see Section B), hence velocity measurements are highly uncertain and this is reflected in the range of values. At later times, as lines de-blend, it becomes easier to associate a particular feature with a particular line.

Fig. 13 plots the line velocities derived the absorption minima of the features with their associated labels. It is clear that the Fe II velocity is higher than any other measured line at the very earliest epoch (35 000 ± 10 000 km s^{-1}, modelling suggests 26 000 km s^{-1} at −13.1 d) and, throughout the ∼55 d period over which we make measurements, remains the highest velocity line with the possible exception of Ca II, where the earliest measurement of this feature indicates similar line velocities. The projection of Fe, a heavy ion, to high velocities seems counter-intuitive as the lighter elements could be expected to be in the outer layers of the ejecta. In the case of GRB-SNe iron-group elements can be ejected to high velocities as part of a jet (Ashall et al. 2017). Alternatively, because a small abundance of Fe is required to provide opacity, it could be a consequence of dredge-up of primordial material. Past maximum it appears that Ca II and Fe II diverge but note that for the most part both features still show some significant broadening, as indicated by the error bars. As the Ca II NIR triplet is a series of lines, and it is hard to attribute the minimum to exactly one line, then it is likely that Fe II and Ca II form lines at similar velocities. This was noticed in Prentice & Mazzali (2017) for other He-poor SNe. The Fe II line finds a plateau at ∼16 000 km s^{-1} around t_{max} while for Ca II this value is ∼14 000 km s^{-1}.

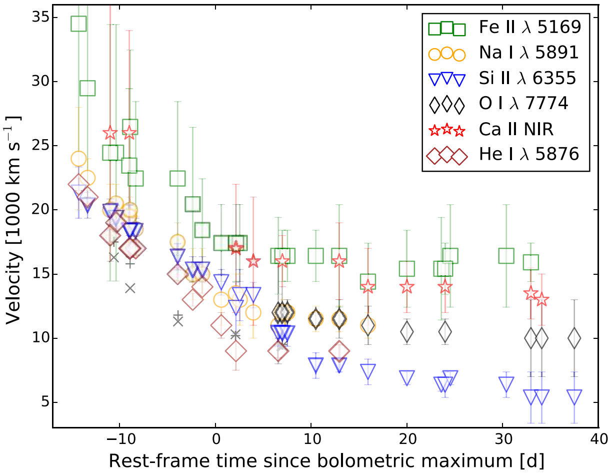

Figure 13. The line velocities of SN 2016coi as measured from absorption minima. Error bars represent the valid spread of velocities that the line could take and, as discussed in the text, we caution against taking line velocities from blended lines. Before peak it appears that the line-forming region for CaII and Fe II occurs at a similar velocity coordinate, and the same can be said for Si II and Na I/He I. As the photosphere recedes the apparent ejecta stratification becomes clear with Fe II and Ca II retaining high velocities, Na I/He I and O I occupying the same shell, and Si II splitting further. He I closely traces the photospheric velocity v_{ph}, as derived in Section 7. In those models, however, the ∼5400 Å feature is dominated by NaI by maximum light. Thus, the detection of He, and subsequent velocities, are tenuous at this time.

The velocity of He I λ 5876 is measured from the same absorption feature as Na I D. However, there is an additional constraint on the range of valid velocities for helium as the He I λλ 6678, 7065 lines must also match features in the spectra. This means that the position in the absorption feature used to measure velocity varies between He I λ5876 and Na I D, hence differing velocity evolutions, as can be seen in Fig. 13.

The Na I D/He I and Si II lines follow a very similar evolution until near t_{max}. If the ∼5500 Å is assumed to be Na I, then these remain similar until around a week after maximum at which point SiII appears to level off at around 6000 km s^{-1} while Na I levels off at ∼12 000 km s^{-1}. It appears that there is a shell of material that is mixed Na and Si. When the photosphere recedes far enough, the base of the Na layer is revealed and the two velocities decouple. If the feature is He I then the He I velocities remain around or just below Si II and He I has a sharper velocity gradient than Si II. He I then levels off at ∼9000 km s^{-1} around t_{max}. In He-rich SNe He I, Ca II, and Fe II are typically found at similar velocities, above that of Si II and O I.

A week after t_{max} is also the first opportunity to estimate O I as it has de-blended from the Ca II NIR triplet, and it can be seen that the line velocity matches that of Na I. Given that the O I velocity is below that of the earlier Na I and Si II velocities, we can suggest that there is a shell in the ejecta which contains all three elements, this may also include He.

Fig. 14 presents comparison of the line velocities with He-poor SNe, marked according to classification. The velocities of SN 2016coi are comparable to other Ic-3/4 SNe.

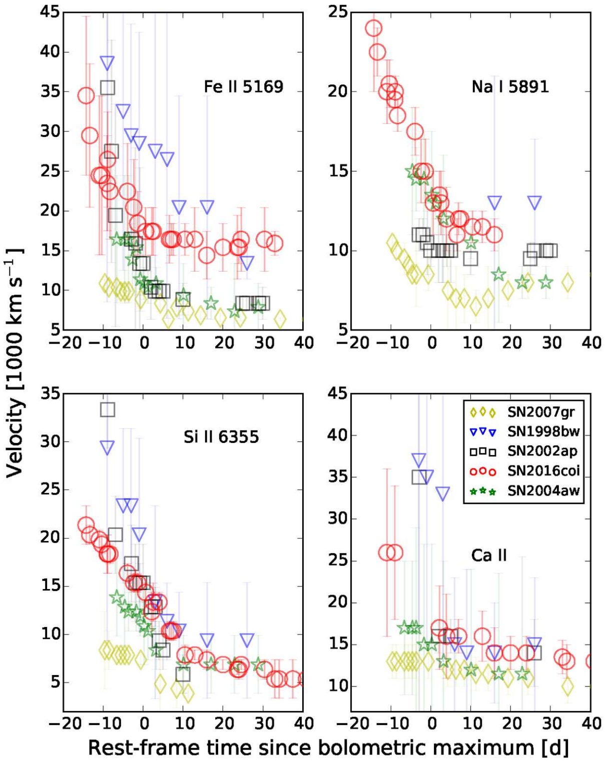

Figure 14. Comparative line velocities between different He-poor SNe types, measured as per Fig. 13. Included are Ic-3 GRB SN 1998bw (blue), Ic-4 SN 2002ap (black), Ic-6 SN 2004aw (green), Ic-7 SN 2007gr (yellow), and SN 2016coi (red). Difficulties with measuring velocities of highly blended lines are discussed in the text; this is why the line velocities of SN 1998bw can appear discontinuous.

7 MODELLING

7.1 The photospheric phase

To determine the elements which make up the spectra, and to examine the range of possible values for $E(B-V)_{\rm host}$, we turn to spectral modelling. This technique utilizes the fact that SNe are in homologous expansion within a day of explosion, such that $r = v_{\rm ph} \times t_{\rm exp}$ where r is the radial distance, $v_{\rm ph}$ is the photospheric velocity, and $t_{\rm exp}$ is the time of explosion. We use a 1D Monte Carlo spectra synthesis code (see Abbott & Lucy 1985; Mazzali & Lucy 1993; Lucy 1999; Mazzali 2000), which follows the propagation of photon packets through an SN ejecta.

The code makes use of the Schuster–Schwarzschild approximation, which assumes that the radiative energy is emitted from an inner boundary blackbody. This approximation is useful, as it does not require in-depth knowledge of the radiation transport below the photosphere, while it still produces good results. The code works best at early times, when most of the ^{56}Ni is located below the photosphere. At late times significant gamma-ray trapping occurs above the photosphere, and the assumption of the model begins to break down. This code has been used to model SNe Ia (e.g. SNe 2014J and 1986G Ashall et al. 2014, 2016), SE-SNe (e.g. SNe 1994I and 2008D Sauer et al. 2006; Mazzali et al. 2008), and GRB-SNe (e.g. SNe 2003dh and 2016jca Mazzali et al. 2003; Ashall et al. 2017).

The photon packets have two possible fates; they either re-enter the photosphere, through a process known as back scattering or escape the ejecta and are 'observed'. Packets can undergo Thomson scattering and line absorption. If a photon packet is absorbed it is re-emitted following a photon branching scheme which allows both fluorescence (blue to red) and reverse fluorescence (red to blue) to take place. A modified nebular approximation is used to treat the ionization/excitation state of the gas, to account for non-local thermodynamic equilibrium (NLTE) effects. The radiation field and state of the gas are iterated until convergence is reached. The final spectrum is obtained by computing the formal integral. Non-thermal effects can be simulated in the code in a parametrized way through the use of departure coefficients, which modify the populations of the excited levels of the relevant ions (e.g. Mazzali et al. 2009). To treat He I, we use departure coefficients of 10^4 (Lucy 1991; Mazzali & Lucy 1998; Hachinger et al. 2012). The purpose of the code is to produce optimally fitting synthetic spectra, by varying the elemental abundance, photospheric velocity and bolometric luminosity. The code requires an input density profile, which can be scaled in time to the epoch of the spectrum, due to the homologous expansion of the ejecta.

As SN 2016coi shows spectroscopic similarity to Ic-4 SN 2002ap, but with a LC width which is ∼40 per cent larger, we use the same density profile that was used to model SN 2002ap (Mazzali et al. 2002), but scaled up in $M_{\rm ej}$ by 40 per cent. The calculated $M_{\rm ej}$ is 2.5–4 $\rm M_{\odot}$ with a $E_{\rm k} = (4.5–7) \times 10^{51}$ erg, with a specific kinetic energy $E_{\rm k}/M_{\rm ej}$ of $\sim$1.6 [10^{51} erg/$\rm M_{\odot}$] throughout (see Mazzali et al. 2017 for a discussion on uncertainties in spectral modelling).

7.1.1 *Investigating* E(B − V)*host*

As discussed in Section 3, $E(B-V)_{\rm host}$ is very uncertain. Therefore, we produced a set of four models at −10.9 d relative to bolometric maximum and 5.4 d from explosion (see Fig. 15). The models have varying $E(B-V)_{\rm host}$= 0.05, 0.10, 0.15, and 0.2 mag. It is apparent that most of the models produce reasonable fits, but the model with $E(B-V)_{\rm host}$= 0.2 mag is too hot and has a slightly worse fit (i.e. there is not enough absorption in the features at 4200 and 4700 Å). Also, the model with $E(B-V)_{\rm host}$ = 0.05 mag, similar to that derived from the interstellar Na I D absorption, produces acceptable fits. However, other properties (i.e. $g-r$ colour curve and Ni mass to ejecta mass ratio) of SN 2016coi are in tension with this value of the extinction. Therefore, we choose to take a value of $E(B-V)_{\rm host}$ of 0.125 mag, which is in-between the two best fits ($E(B-V)_{\rm host}$ = 0.1 & 0.15 mag). This value of $E(B-V)_{\rm host}$ also provides good spectral fits (see the middle panel of Fig. 15).

7.1.2 *Modelling results*

With the distance, extinction, and density profile determined, we produced spectral models at five different epochs ($t_{\rm exp}$ = 5.4, 7.1, 12.1, 18.1, and 23.0 d) to determine which ions contribute to the formation of the spectra and abundances. We do this both with and without He, and discuss the faults and merits with both sets of models. The basic input parameters of the models are presented in Table 5. When determining the properties of an SN spectrum, it is important to have the correct flux level in the UV/blue, as there is re-processing of flux from the blue to the red due to the Doppler overlapping of the spectral lines. This process is known as line blanketing, a process by which photon packets only escape the SN ejecta in a 'line free' window, which is always redward from where they are emitted.

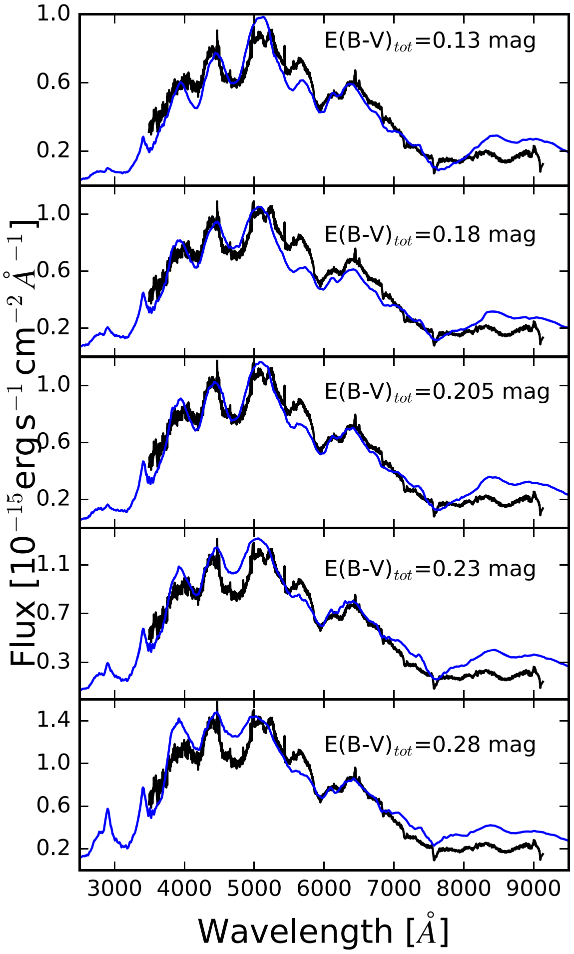

Figure 15. A set of models (blue) produced at t = 5.4 d after explosion compared with the −10.9 d spectrum (black). The observations have been corrected for different amounts of host galaxy extinction in addition to $E(B-V)_{\rm MW}$ = 0.08 mag, and a model produced for each spectrum. The best fits suggest $E(B-V)_{\rm host}$ is 0.1–0.15 mag, greater than this and the luminosity requires a higher temperature which changes the ionization regime of the spectra.

Table 5. Basic parameters of models form Fig. 16.

		No He		With He	
$t_{\rm exp}$ (d)	$t - t_{\rm max}$ (d)	UVOIR $\log_{10}$ ($L_{\rm p}$/erg s^{-1})	$v_{\rm ph}$ (km s^{-1})	UVOIR $\log_{10}$ ($L_{\rm p}$/erg s^{-1})	$v_{\rm ph}$ (km s^{-1})
5.4	− 10.6	42.08	16 300	42.08	17 500
7.1	− 8.9	42.26	13 900	42.31	15 800
12.1	− 3.9	42.48	11 300	42.49	11 800
18.1	+2.1	42.58	10 300	42.54	10 200
23.0	+7.0	42.52	9400	42.53	9500

7.2 Models without He

The right-hand panel in Fig. 16 presents the spectral models of SN 2016coi without He. The main ions are labelled at the top of the panel, and the same lines tend to form the spectra at all epochs. The photospheric velocity covers a range of 9400–16300km s^{-1}, and the bolometric luminosities are roughly consistent with those derived in Section 5. The blue part of the spectrum consists of Mg II resonance lines (λλ2803, 2796), the CaII ground state lines (λλ3968, 3934), as well as blends of metals including CoII lines, the strongest of which are λλ 3502, 3446, 3387. The feature at ∼4200 Å, is dominated by Mg II (λλ4481.13, 4481.32), CoII (λλ4569, 4497, 4517) and FeII (λ4549). The feature at ∼4700 Å consists of a blend of FeII (λλ5169 5198), SiII (λλ5056 5041) and CoII (λλ5017, 5126, 5121, 4980). At ∼5600 Å absorption is caused by NaI (λλ5896 5890), and the small absorption on the red-ward side of the feature is produced by SiII (λλ5958,5979). SiII (λλ6347, 6371) forms the spectra at, ∼6000 Å, and the smaller feature at ∼6300 Å is produced by CII (λλ 6578, 6583). The notch at ∼6700 Å is produced by Al II (λλ7042, 7056.7, 7063.7), there is also CII (λ7236, 7231) absorption in the same wavelength range as the telluric feature at ∼6900 Å. The broad feature at ∼7500 Å is a blend of CaII (λλ8498, 8542, 8662) and OI (λλ7771, 7774, 7775). Finally, the feature at ∼8700 Å is dominated by MgII (λλ9218, 9244). Although these models produce a good fits, arguably better than those with He, the abundances we require for Al and Na are unusual (see Section 7.4) and are an argument against these line identification.

7.3 Models with He

The left panel in Fig. 16 contains the spectral models of SN 2016coi with He. The main ions which contribute to each feature are labelled at the top of the plot, and the basic input parameters can be found in Table 5.

The models are similar to those without helium except now the feature at ∼4200 Å, contains He I (λλ4471.47, 4471.68, 4471.48, 4388), the one at ∼4700 Å has HeI (λλ4923 5016), and the feature at ∼5600 Å consist of only HeI (λλ5875.61, 5875.64, 5875.96, 5875.63) at $t_{\rm exp}$ = 5.4 d, although the small absorption on the red-ward side of the feature is Si II (λλ5958,5979).

The notch at ∼6700 Å is produced by He I (λλ7065.17, 7065.21, 7065.70) absorption, and there is HeI (λ7281) and CII (λλ7236, 7231) absorption in the same wavelength range as the telluric feature at ∼ 6900 Å.

For these models the line identification was made at $t_{\rm exp}$ = 5.4 d. However, it should be noted that by $t_{\rm exp}$ = 18.1 d (∼2 d after maximum light) the dominant ion in the ∼5600 Å feature is Na I, and the dominant ion in the ∼ 6300 Å feature is C II. This could however change if the departure coefficients were different. For example Hachinger et al. (2012) determined that at 22.1 d past maximum light, the departure coefficients in the deep atmosphere layers were $\sim 10^3$, but in the outer atmosphere layers they were $\sim 10^7$. So it could be the case that He absorption could produce these features at later times if the departure coefficients are increased. However, in the observations these ‘He’ features do disappear over time, unlike in SNe Ib, and in other SNe Ic (such as 2002ap) Na I appears ∼3 d before peak, some 7–10 d after explosion.

He excitation usually increases with time as more non-thermal particles penetrate through the SN ejecta. In this case, He lines are possibly present early on but do not grow in strength over time, rather the opposite. This suggest that there is only a very small amount of He in the outer layers of the exploding star, and that there may be some ^{56}Ni mixed out to high velocities to non-thermally excite the lines at early times. At later times, as density decreases, the opacity in the outer layers is too small for the deposition of fast particles, even when locally produced.

7.4 Abundances

7.4.1 The He free models

The bottom panel of Fig. 17 shows the abundances as a function

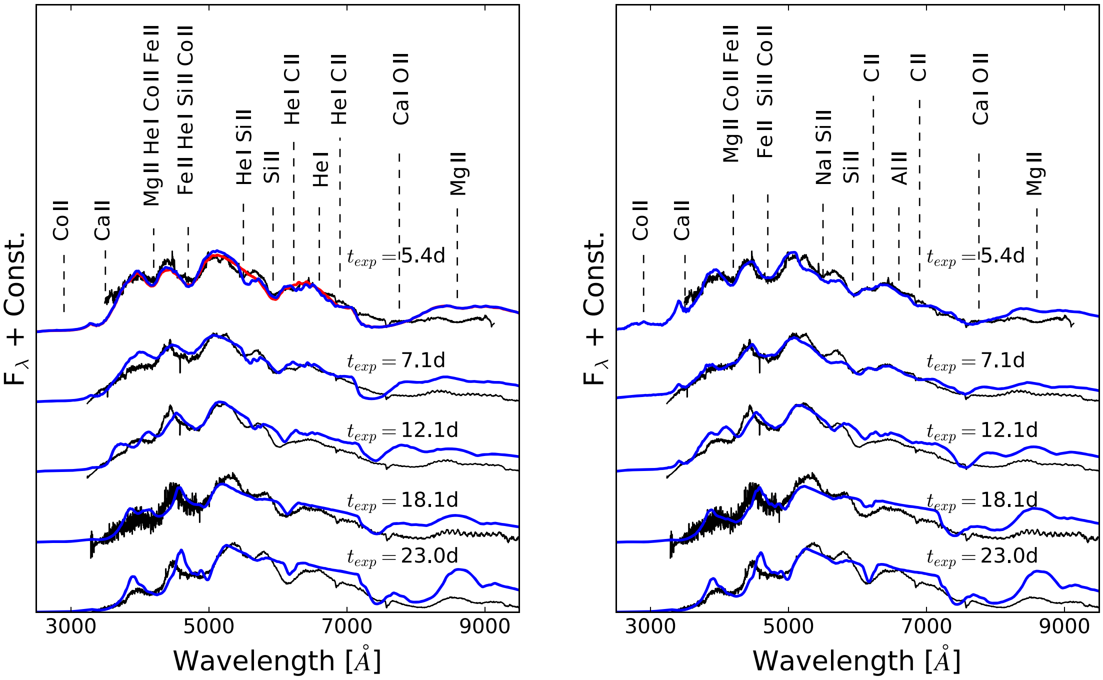

Figure 16. A time series of spectral models (blue) and observations (black) at five different epochs. *Left:* The models were produced with He enhanced with departure coefficients. The red model at $t = 5.4$ d is the same as the blue model but with no departure coefficient applied, demonstrating that the He I lines need to be non-thermally excited. *Right:* spectral models with no He abundance.

of velocity for the models that do not include He. The abundances here are generally consistent with the explosion of a C/O core of a massive star, with a few exceptions. The Na abundance is ~6 per cent, given that Na is not produced in a SE-SN explosion, this Na must come from the progenitor system. However, the metallicity of UGC 11868 is approximately one third solar, and the solar abundance of Na is $\sim 1 \times 10^{-6}$ (Asplund et al. 2009). Therefore, it seems physically unlikely that there could be this much Na in this object. Furthermore, the average Al abundance is ~0.6 per cent, This is much larger than the solar value of $\sim 2 \times 10^{-6}$, demonstrating that these line identifications are unlikely.

7.4.2 The models with He

The top panel in Fig. 17 shows the abundances in velocity space for the models that include He. These abundances are consistent with what could be expected from a core of a massive C/O star. Carbon dominates at the highest velocity, and oxygen at lower velocities. The Na abundance in this model is about $\sim 3 \times 10^{-5}$, which is more consistent with solar values, and no Al is required for this model. The abundance of He decreases as a function of velocity, this coincides with the decreasing strength of the He features in the models. The outer layers (at $v_{\rm ph}$= 17 500km s^{-1}) have a He abundance of 3 per cent, whereas when the photosphere has receded to 9400 km s^{-1} the He abundance is 0.1 per cent. As time passes, it should become easier for non-thermal electrons, energized by gamma-rays from ^{56}Ni decay, to reach the He layer and excite He into the states required to produce lines in the optical. However, the small abundance of He in the outer layers, which gets more diffuse as time increases, means that at later times there would be no indication of He in the spectra because the He opacity is insignificant.

In conclusion, the models indicate that the debated lines could be produced by Na and Al or from He, but the abundances from our models suggests that the He identification is more likely.

7.5 Models of the nebular phase

We modelled the nebular-epoch spectrum of SN 2016coi using our non-local thermodynamic equilibrium (NLTE) code. This code has been described extensively in Mazzali et al. (2007) and used for both SNe Ia and Ib/c (e.g. Mazzali et al. 2017). It computes the energy produces in gamma-rays and positrons by radioactive decay of ^{56}Ni into ^{56}Co and then ^{56}Fe, it then follows the propagation of the gamma-rays and positrons in the SN ejecta, computes the heating caused by the collisions that characterize the thermalization of these particles, and balances it with cooling via line emission. Both permitted and forbidden transitions can be sources of cooling. An emerging spectrum is computed based on line emissivity and a geometry which can either be stratified in abundance and density or a single zone, which is then bounded by an outer velocity.

In the case of SN 2016coi we simply use the one-zone model, as we aim at getting an approximate value of the ^{56}Ni mass and the emitting gas. In SNe Ic the emitting mass is mostly oxygen, and the range can be from less than 1 M$_\odot$ (SN 1993J Sauer et al. 2006) to about 10 M$_\odot$ in GRB-SNe like 1998bw (Mazzali et al. 2001) to several dozen M$_\odot$ in PISN candidates like SN 2007bi (Gal-Yam et al. 2009).

The optical spectrum of SN 2016coi can be reproduced by an emitting nebula with outer boundary velocity 5000 km s^{-1} and mass ~1.50 M$_\odot$ within that velocity (Fig. 18). The ^{56}Ni mass required to heat the gas is 0.14 M$_\odot$, which makes SN 2016coi as luminous as most SNe Ic, but significantly less luminous than GRB/SNe. The ^{56}Ni mass is verified also by the flux in the forbidden [Fe II] lines near 5200 Å. The oxygen mass, as determined by the emission at λλ6300,

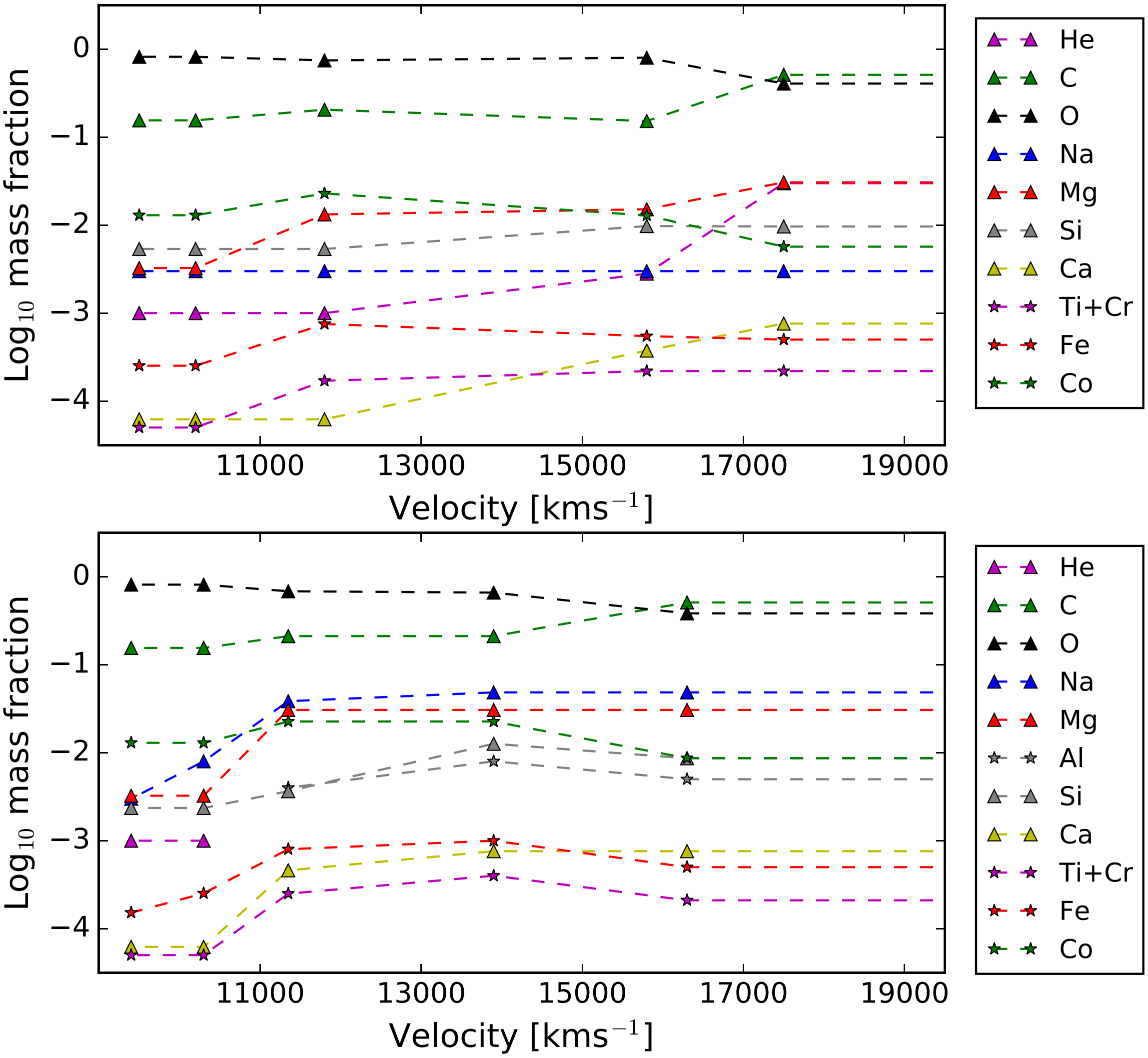

Figure 17. Abundance as a function of velocity for models presented in the previous figure. The top panel corresponds to the models with He, and the bottom to the models without He.

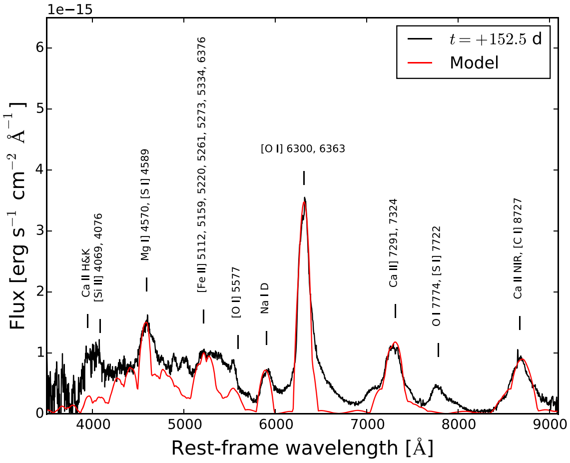

Figure 18. The nebular model of SN 2016coi (red) with the +152.5 d spectrum (black)

6363 is 0.75 M$_\odot$. Some unburned carbon is also present. C I λ8727 contributes to the red wing of the Ca-dominated emission near 8600 Å, and the mass required is 0.12 M$_\odot$. Calcium produces strong emission lines, esp. the semiforbidden Ca II] $\lambda\lambda$7290, 7324, but also H&K $\lambda\lambda$3933, 3968 and the IR triplet near 8500 Å. These are intrinsically strong lines, so that a small mass of Ca, $\sim$0.005 M$_\odot$, is sufficient. Other strong lines are due to magnesium ([Mg I λ4570) and sodium (Na I D λ5890), but the masses of these elements are quite small ($\sim 2 \times 10^{-3}$ and 2×10^{-4} M$_\odot$, respectively) Finally, the mass of the most abundant intermediate-mass elements, silicon and sulphur, can be determined indirectly. For Si, the model should not exceed the observed emission near 6500 Å, which could be Si I] λ6527, which sets a limit of $\sim$1.50 M$_\odot$ and leads to a strong emission near 1.6 µm, while for sulphur the strongest optical line is S II] λ4069, which is well reproduced for a mass of 0.12 M$_\odot$, leading to strong NIR emission near 1.1 µm. It is unusual for the Si/S ratio to be as large as 10 or more, so if the upper limit for sulphur is established silicon should probably not exceed $\sim$0.5 M$_\odot$. The availability of NIR data would improve the constraints on these elements. The model does not use clumping. If clumping is used, a slightly worse ratio of the permitted and semi-forbidden Ca II] lines is produced, suggesting that the density is too high in that case.

On the other hand, photospheric phase modelling indicates that the mass enclosed within 5000 km s^{-1} should be ∼1 M$_{\odot}$. As oxygen and ^{56}Ni alone already reach almost that value, this suggests that the mass of silicon and sulphur should be small. A reasonable match to the late-time spectrum can be found for a ^{56}Ni mass of 0.14 M$_{\odot}$, an oxygen mass of 0.75 M$_{\odot}$, carbon 0.11 M$_{\odot}$, calcium 0.005 M$_{\odot}$. This model has a very weak NIR flux. If the bluest part of the spectrum is not well calibrated the poor apparent fit to the Ca II H&K and S I] emissions does not constitute a problem. The model does not use clumping.

8 DISCUSSION

8.1 Helium

Yamanaka et al. (2017) claimed detection of He in the early spectra of SN 2016coi initially. Here, we consider the evidence based on our own analysis. In the first instance we consider the arguments for He:

(i) Several absorption features line up with prominent He lines in the early spectra.

(ii) Using a sensible departure coefficient, our spectral models can include realistic quantities of He.

(iii) Abundance estimates for other likely ions, in particular Na and Al, disfavour these elements having a strong contribution at early times

(iv) The very early spectra show more absorption features than other 'broad-lined' SNe, suggesting the nature of this object is a little different

However, there are also reasons to doubt this identification.

(i) The He lines do not behave as they do in He-rich SNe as the lines decay in strength over time rather than increase in strength (e.g. Liu et al. 2016; Prentice & Mazzali 2017).

(ii) The features attributed to He I do not share the same shape, suggesting that they are not tracing the same line-forming region. In He-rich SNe the shape of the He I λλ6678, 7065 lines are extremely similar

(iii) The velocity of He in relation to other elements is unlike that in He-rich SNe where He is found to have the highest ejecta velocity (or second highest if H is present). We instead find that the prominent ∼5400 Å feature attributed to He I λ5876 shows a velocity similar to Si II.

(iv) If the ∼5400 Å feature remains He dominated after maximum then it levels off to a velocity lower than that of Fe II and Ca II.

Thus, we have a model which suggests that there may be a small amount of He in the ejecta, but its behaviour is unlike that in any He-rich SN. NIR spectra would aid in the identification of helium as He I λ 2.058 µm is a strong line that is somewhat isolated from other prominent features. If He is present, then the progenitor appears to have been almost completely stripped of it prior to explosion, leaving some residual amount to imprint on the spectra.

8.2 Classification

The classification of SN 2016coi is complicated by the uncertain presence of He in the ejecta, Yamanaka et al. (2017) took the view that this was a broad-lined type Ib. In the previous section, however, it was noted that the identification of He is promising, but not conclusive. In Prentice & Mazzali (2017), two methods for classifying SE-SNe were presented for He-rich and He-poor SNe. In that work, no SE-SNe was found to have just a small quantity of He present, it was either clearly there or absent. There are more than a dozen examples of SNe classified as type Ic with spectroscopy earlier than a week before maximum light, when features akin to those in SN 2016coi would be visible. It is unexplained how the envelope stripping process could leave a clear distinction between SNe with enough He to form strong lines and no He. If SN 2016coi was to have He in the ejecta then would this represent a unique intermediate case? This seems unlikely, as our results suggest that if there is He present in the ejecta it is not in the form of a He shell, but a result of some mixing into the C/O layer below this (as per the line velocities). It may be the case here that residual He is non-thermally excited by ^{56}Ni mixed into the outer layers but the abundance is so small that it rapidly becomes too diffuse to further influence line formation. Indeed, the velocity of He I lines closely follows that of the photosphere. This may also suggest that because ^{56}Ni mixing is expected to occur in SNe Ic, especially those with broad lines, and because these features are not seen then they are genuinely free of He.

SN 2016coi is spectroscopically similar to Ic-4 SNe around peak, regardless of the arguments for and against the presence of He. Thus, based upon the method for SN classification presented in Prentice & Mazzali (2017), we classify SN 2016coi as Ic-4(14/21) where 4 is the mean number of features visible in the spectra at $t_{-1/2}$ and $t_{\rm max}$, 14 is the velocity of the Si II line at $t_{\rm max}$ in units of 1000 km s^{-1} (see Section 6.2.1), and 21 is $t_{+1/2}$ in units of rest-frame days. This classification system provides a quick reference to compare He-poor SNe line blending and physical properties.

The typical specific kinetic energy of Ic-4 SNe is ∼2, but they show a wide range of $L_{\rm p}$, $E_{\rm k}$, and $M_{\rm ej}$, as well as temporal parameters. SN 2002ap is relatively dim, had low $M_{\rm ej}$ ∼2.5 $M_{\odot}$ and $E_{\rm k}$ ∼4 × 10^{51}erg, whereas Ic-4 SN 1997ef had $M_{\rm ej}$ ∼8 M$_{\odot}$ and $E_{\rm k}$ ∼16 × 10^{51} erg. SN 2016coi sits between the two with $M_{\rm ej}$ = 4–7 M$_{\odot}$, $E_{\rm k}$ = (4.5–7) × 10^{51} erg and $E_{\rm k}/M_{\rm ej}$ ∼1.6 [10^{51} erg/M$_{\odot}$].

A final point on the classification is that as more examples of this type of SN are discovered, and if the presence of He is confirmed, then the taxonomy should be adjusted to account for these objects and their physical parameters. We suggest that the scheme from Prentice & Mazzali (2017) could be adapted to account for this by referring to such SNe as Ic(b)-⟨N⟩.

9 CONCLUSIONS

We have presented the photometric and spectroscopic evolution of type Ic-4(14/21) SN 2016coi for around 460 d, from shortly after explosion until the nebular phase. Our dense sample of 56 spectra has allowed us to trace the evolution of features within the SN and the transition to the nebular phase in unprecedented detail. It has been found that the SN has quite typical light curve parameters in comparison with other non-GRB associated type Ic events with a *griz* pseudo-bolometric $L_{\rm p}$ = (1.9 ± 0.1) × 10^{42} erg s^{-1}and *ugriz* $L_{\rm p}$ = (2.4 ± 0.1) × 10^{42}, and an estimated total bolometric UVOIR luminosity of $L_{\rm p}$∼3 × 10^{42}. The *griz* temporal parameters, with $t_{-1/2}$ = 12.4 ± 0.5 d and $t_{+1/2}$ 23 ± 1 d, are a little more extreme than normal SNe Ic but not as extreme as the broadest SNe Ic. The SN follows a late time decay rate (non-host subtracted) of 0.015 mag d^{-1}. The SN synthesized ∼0.14 $M_{\odot}$ of ^{56}Ni based upon the estimated UVOIR light curve peak and the results of spectral modelling (contrasting with ∼0.09 $M_{\odot}$ from the *griz* $L_{\rm p}$ alone). We note that there is significant uncertainty in the distance to the SN and the value of $E(B-V)_{\rm host}$. We have attempted to constrain these properties where possible but accept that $M_{\rm Ni}$ and $L_{\rm p}$ are greatly affected by changes to these values.

Spectroscopically, the SN shows broad absorption features common the Ic-3/4 SNe, but a strong absorption around ∼5400 Å in the early spectra is unusual. This feature, in conjunction with weaker features at ∼6100 and ∼6500 Å, suggests the presence of helium in the ejecta. However, spectral models and observational evidence indicates that if this is He then it is in very low quantities and located at low velocities in a C/O dominated shell. It becomes diffuse quickly as the lines weaken with strength towards maximum light, contrary to the behaviour of the lines in He-rich SNe. By ∼ +2 d the feature is dominated by Na. We conclude that the SN is a 'broad-lined ' type Ic that likely retains trace He mixed in the a C/O dominated shell, which is non-thermally excited at early times by ^{56}Ni projected into the outer layers. It does not represent a case of an SN Ib with weak He lines.

Spectral models indicate that SN had $E_{\rm k} = (4.5\text{–}7) \times 10^{51}$ erg and $M_{\rm ej} = 2.5\text{–}4\,{\rm M}_{\odot}$, with ∼1.5 $\rm M_{\odot}$ below 5000 km s^{-1}. This makes SN 2016coi one of the more massive He-poor SE-SNe and similar to Ic-6 SN 2004aw (Mazzali et al. 2017). The host is LMC-like, and the SN exploded away from star-forming regions. Additionally, we suggest that the metallicity of the host is similar to that of the LMC. From this and $M_{\rm ej}$, we estimate that the progenitor, likely a Wolf–Rayet star at the time of explosion, had $M_{\rm ZAMS} = 23\text{–}28\,{\rm M}_{\odot}$.

ACKNOWLEDGEMENTS

SJP and CA are funded by a Science and Technology Facilities Council (STFC) grant. CA acknowledges the support provided by the National Science Foundation (NSF) under Grant No. AST-1613472. The LT is operated on the island of La Palma by Liverpool John Moores University in the Spanish Observatorio del Roque de los Muchachos of the Instituto de Astrofisica de Canarias with financial support from the STFC. This paper makes use of data from Las Cumbres Observatory and the Supernova Key Project. DAH, CM, and GH are supported by NSF grant number 1313484. Research by DJS and L.T. is supported by NSF grant AST-1412504 and AST-1517649. Research at Lick Observatory is partially supported by a generous gift from Google. Funding for the Lijiang 2.4 m telescope (LJT) has been provided by the Chinese Academy of Sciences (CAS) and the People's Government of Yunnan Province. The LJT is jointly operated and administrated by Yunnan Observatories and Center for Astronomical Mega-Science (CAS). J.-J. Zhang is supported by National Science Foundation of China (NSFC, grants 11403096 and 11773067), the Youth Innovation Promotion Association of the CAS, the Western Light Youth Project, and the Key Research Program of the CAS (grant no. KJZD-EW-M06). Finally, we thank the anonymous referee for their time, consideration, and patience.

REFERENCES

Abbott D. C., Lucy L. B., 1985, ApJ, 288, 679
Arcavi I. et al., 2011, ApJ, 742, L18
Arnett W. D., 1982, ApJ, 253, 785
Ashall C. et al., 2017, preprint (arXiv:1702.04339)
Ashall C., Mazzali P., Bersier D., Hachinger S., Phillips M., Percival S., James P., Maguire K., 2014, MNRAS, 445, 4427
Ashall C., Mazzali P. A., Pian E., James P. A., 2016, MNRAS, 463, 1891
Asplund M., Grevesse N., Sauval A. J., Scott P., 2009, ARA&A, 47, 481
Barnsley R. M., Smith R. J., Steele I. A., 2012, Astron. Nachr., 333, 101
Beasor E. R., Davies B., 2016, MNRAS, 463, 1269
Becker A., 2015, Astrophysics Source Code Library, record ascl:1504.004
Berg D. A. et al., 2012, ApJ, 754, 98
Bianco F. B. et al., 2014, ApJS, 213, 19
Brown T. M. et al., 2013, PASP, 125, 1031
Cardelli J. A., Clayton G. C., Mathis J. S., 1989, ApJ, 345, 245
Cioni M.-R. L., 2009, A&A, 506, 1137
Clocchiatti A., Wheeler J. C., 1997, ApJ, 491, 375
Corsi A. et al., 2011, ApJ, 741, 76
Corsi A. et al., 2012, ApJ, 747, L5
de Vaucouleurs G., de Vaucouleurs A., Corwin H. G., Jr, Buta R. J., Paturel G., Fouqué P., 1991, Third Reference Catalogue of Bright Galaxies. Volume I: Explanations and references. Volume II: Data for galaxies between 0^h and 12^h. Volume III: Data for galaxies between 12^h and 24^h
Drout M. R. et al., 2011, ApJ, 741, 97
Drout M. R. et al., 2016, ApJ, 821, 57
Eldridge J. J., Maund J. R., 2016, MNRAS, 461, L117
Eldridge J. J., Fraser M., Maund J. R., Smartt S. J., 2015, MNRAS, 446, 2689
Elias-Rosa N. et al., 2016, MNRAS, 463, 3894
Faber S. M. et al., 2003, in Iye M., Moorwood A. F. M., eds, Proc. SPIE Conf. Ser. Vol. 4841, Instrument Design and Performance for Optical/Infrared Ground-based Telescopes. SPIE, Bellingham, p. 1657
Fan Y.-F., Bai J.-M., Zhang J.-J., Wang C.-J., Chang L., Xin Y.-X., Zhang R.-L., 2015, Res. Astron. Astrophys., 15, 918
Filippenko A. V. et al., 1995, ApJ, 450, L11
Folatelli G. et al., 2014, ApJ, 792, 7
Foley R. J., Berger E., Fox O., Levesque E. M., Challis P. J., Ivans I. I., Rhoads J. E., Soderberg A. M., 2011, ApJ, 732, 32
Fox O. D. et al., 2014, ApJ, 790, 17
Fukugita M., Ichikawa T., Gunn J. E., Doi M., Shimasaku K., Schneider D. P., 1996, AJ, 111, 1748
Gal-Yam A. et al., 2009, Nature, 462, 624
Georgy C., Ekström S., Meynet G., Massey P., Levesque E. M., Hirschi R., Eggenberger P., Maeder A., 2012, A&A, 542, A29
Hachinger S., Mazzali P. A., Taubenberger S., Hillebrandt W., Nomoto K., Sauer D. N., 2012, MNRAS, 422, 70
Helmboldt J. F., Walterbos R. A. M., Bothun G. D., O'Neil K., de Blok W. J. G., 2004, ApJ, 613, 914
Hoeflich P. et al., 2017, ApJ, 846, 58
Holoien T. W.-S. et al., 2016, Astron. Telegram, 9086
Huang F., Li J.-Z., Wang X.-F., Shang R.-C., Zhang T.-M., Hu J.-Y., Qiu Y.-L., Jiang X.-J., 2012, Res. Astron. Astrophys., 12, 1585
Iwamoto K. et al., 1998, Nature, 395, 672
James P. A. et al., 2004, A&A, 414, 23
Jordi K., Grebel E. K., Ammon K., 2006, A&A, 460, 339
Kilpatrick C. D. et al., 2017, MNRAS, 465, 4650
Langer N., 2012, ARA&A, 50, 107
Liu Y.-Q., Modjaz M., Bianco F. B., Graur O., 2016, ApJ, 827, 90
Lucy L. B., 1991, ApJ, 383, 308
Lucy L. B., 1999, A&A, 345, 211
Maeda K. et al., 2008, Science, 319, 1220
Maeda K. et al., 2015, ApJ, 807, 35
Maund J. R. et al., 2015, MNRAS, 454, 2580
Maund J. R., Smartt S. J., Kudritzki R. P., Podsiadlowski P., Gilmore G. F., 2004, Nature, 427, 129
Mazzali P. A. et al., 2002, ApJ, 572, L61
Mazzali P. A. et al., 2003, ApJ, 599, L95
Mazzali P. A. et al., 2006, ApJ, 645, 1323
Mazzali P. A. et al., 2007, ApJ, 670, 592
Mazzali P. A. et al., 2008, Science, 321, 1185
Mazzali P. A. et al., 2014, MNRAS, 439, 1959
Mazzali P. A., 2000, A&A, 363, 705
Mazzali P. A., Lucy L. B., 1993, A&A, 279, 447
Mazzali P. A., Lucy L. B., 1998, MNRAS, 295, 428
Mazzali P. A., Iwamoto K., Nomoto K., 2000, ApJ, 545, 407

Mazzali P. A., Nomoto K., Patat F., Maeda K., 2001, ApJ, 559, 1047
Mazzali P. A., Deng J., Hamuy M., Nomoto K., 2009, ApJ, 703, 1624
Mazzali P. A., Maurer I., Valenti S., Kotak R., Hunter D., 2010, MNRAS, 408, 87
Mazzali P. A., Walker E. S., Pian E., Tanaka M., Corsi A., Hattori T., Gal-Yam A., 2013, MNRAS, 432, 2463
Mazzali P. A., Sauer D. N., Pian E., Deng J., Prentice S., Ben Ami S., Taubenberger S., Nomoto K., 2017, MNRAS, 469, 2498
Metzger B. D., Margalit B., Kasen D., Quataert E., 2015, MNRAS, 454, 3311
Milisavljevic D. et al., 2015, ApJ, 799, 51
Modjaz M. et al., 2009, ApJ, 702, 226
Modjaz M. et al., 2014, AJ, 147, 99
Modjaz M., Kirshner R. P., Blondin S., Challis P., Matheson T., 2008, ApJ, 687, L9
Modjaz M., Kewley L., Bloom J. S., Filippenko A. V., Perley D., Silverman J. M., 2011, ApJ, 731, L4
Modjaz M., Liu Y. Q., Bianco F. B., Graur O., 2016, ApJ, 832, 108
Nomoto K., Yamaoka H., Pols O. R., van den Heuvel E. P. J., Iwamoto K., Kumagai S., Shigeyama T., 1994, Nature, 371, 227
Piascik A. S., Steele I. A., Bates S. D., Mottram C. J., Smith R. J., Barnsley R. M., Bolton B., 2014, Proc. SPIE 9147, Ground-based and Airborne Instrumentation for Astronomy V. p. 91478H
Pignata G. et al., 2011, ApJ, 728, 14
Podsiadlowski P., Joss P. C., Hsu J. J. L., 1992, ApJ, 391, 246
Poznanski D., Ganeshalingam M., Silverman J. M., Filippenko A. V., 2011, MNRAS, 415, L81
Poznanski D., Prochaska J. X., Bloom J. S., 2012, MNRAS, 426, 1465
Prentice S. J. et al., 2016, MNRAS, 458, 2973
Prentice S. J., Mazzali P. A., 2017, MNRAS, 469, 2672
Ryder S. D. et al., 2018, ApJ, 856, 83,
Sanders N. E. et al., 2012, ApJ, 758, 132
Sauer D. N., Mazzali P. A., Deng J., Valenti S., Nomoto K., Filippenko A. V., 2006, MNRAS, 369, 1939
Schlafly E. F., Finkbeiner D. P., 2011, ApJ, 737, 103
Shappee B. et al., 2014, American Astronomical Society Meeting Abstracts #223, p. 236.03
Shivvers I. et al., 2017, PASP, 129, 054201
Smartt S. J., 2009, ARA&A, 47, 63
Smith N., Gehrz R. D., Hinz P. M., Hoffmann W. F., Hora J. L., Mamajek E. E., Meyer M. R., 2003, AJ, 125, 1458
Steele I. A. et al., 2004, in Oschmann J. M., Jr, ed., Proc. SPIE Conf. Ser. Vol., 5489, Ground-based Telescopes. SPIE, Bellingham, p. 679
Stevance H. F. et al., 2017, MNRAS, 469, 1897
Stritzinger M. D. et al., 2018, A&A, 609, A135
Stritzinger M., Leibundgut B., 2005, A&A, 431, 423
Taddia F. et al., 2015, A&A, 574, A60
Taddia F. et al., 2018, A&A, 609, A136
Tartaglia L. et al., 2017, ApJ, 836, L12
Taubenberger S. et al., 2006, MNRAS, 371, 1459
Tonry J. L. et al., 2012, ApJ, 750, 99
Valenti S. et al., 2016, MNRAS, 459, 3939
Van Dyk S. D. et al., 2014, AJ, 147, 37
Wang X. et al., 2008, ApJ, 675, 626
Woosley S. E., Eastman R. G., Weaver T. A., Pinto P. A., 1994, ApJ, 429, 300
Yamanaka M. et al., 2017, ApJ, 837, 1
Yoon S.-C., Gräfener G., Vink J. S., Kozyreva A., Izzard R. G., 2012, A&A, 544, L11
Zhang J.-J., Wang X.-F., Bai J.-M., Zhang T.-M., Wang B., Liu Z.-W., Zhao X.-L., Chen J.-C., 2014, AJ, 148, 1

APPENDIX A: STATIC FEATURES IN THE SPECTRA

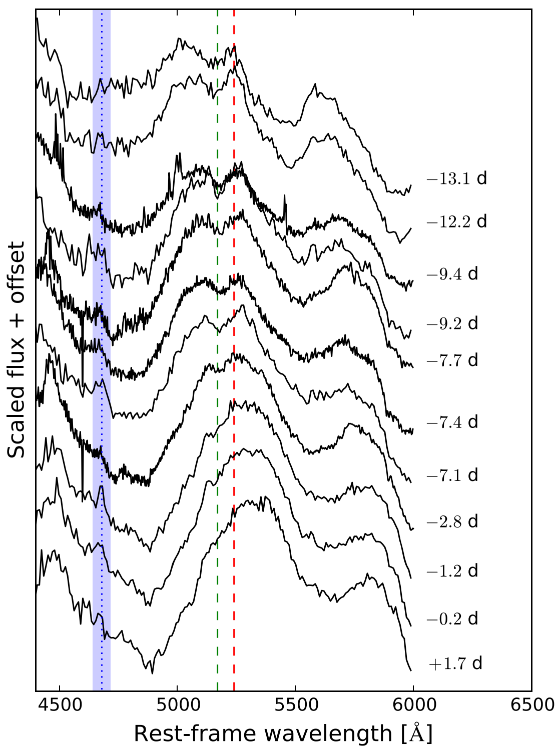

Figure A1. The pre-peak spectra of SN 2016coi showing static features. The blue dotted line and region surrounds a line that may be in emission, this does not move as the absorption feature moves in velocity underneath suggesting that it is external to the SN ejecta. This feature is present in spectra from three different instruments located in China, La Palma, and Hawaii, which suggests it is not noise. The green dashed line and the red dashed line show a feature that is in absorption (green) and possibly emission (dashed). The feature disappears as the pseudo-emission peak moves red-ward.

The early spectra of SN 2016coi show two regions where features appear to be static despite the rapid evolution in line velocity and the degree of blending, they are shown in Fig. A1. Analysis of these features is beyond the scope of this work, but we briefly discuss their effect on the early time spectra.

Aside from the abnormal strength of the absorption ∼5500 Å the early spectra also show an line absorption around ∼5170 Å and a possible re-emission peak at 5240 Å. The absorption is rather weak, and by peak it has disappeared into the absorption caused by the blend of lines blueward of its position. Strangely, the velocity evolution of this line, if any, is also weak, especially compared with how the absorption profiles blueward and redward are decreasing in velocity. At $t = -13.1$ d, the absorption profile looks to be significantly broader than at later times, this however may be deceptive as the S/N of the spectrum masks the true position of the base and the re-emission peak that the absorption profile is sitting on is being narrowed and shifted redward over time but the competing absorption features either side of it.

We can find no explanation for this in the ions normally found in SN ejecta. If the ‘emission’ at 5240 Å is the rest wavelength of the absorption then the line velocity is extremely small ∼4000 Å when compared with other line velocities at this epoch.

There also appears to be a weak ‘emission feature’ around 4670 Å, which is static against the redward movement of the broad absorption feature behind it. The feature does not appear to be systematic as it is present in spectra from SPRAT, Floyds, and LJT. Assuming this feature is some emission line at the rest wavelength then estimate of the half width at half-maximum (∼15–

25 Å) gives a velocity of ∼1000 km s^{-1}. The line disappears as the pseudo-emission peak immediately blueward moves into the same wavelength regime and is not seen again. If the line was the result of recombination from ionized circumstellar medium, it could be attributable to He II λ4686 offset by 1000 km s^{-1}; however, there appears to be no evidence for other emission lines and so we remain sceptical. Note that in the post-peak spectra there is a small pseudo-emission peak in the Fe II blend that is attributable to the de-blending of Fe II λ4924 and λ5018 lines from the Fe II λ5169 line. This is commonly seen in the evolution of SE-SNe.

Recognizing the behaviour of the 4670 Å feature is important because it could be mistaken for a pseudo-emission peak related to the Doppler shifted Fe II λ5018 line. As classification is dependent upon the blending of the three strong Fe II lines in this region (see Section 8.2) then the behaviour of this feature must be catalogued. As the line is static, we can rule out its being a consequence of Fe II.

APPENDIX B: LINE VELOCITY MEASUREMENTS OF BLENDED LINES

Blended lines cause a problem for line velocity measurements as the minima of the absorption features do not necessarily represent a single atomic transition. To demonstrate, we use the spectra of SN 2002ap and measure the velocity of the feature in the region around 4500–5000 Å from the absorption minimum and using the three strong iron transitions in this region; Fe II λλ4924, 5018, 5169. The results are shown in Fig. B1 where it can be seen that it is not possible to define the velocity throughout by the use of a single line, we also show v_{ph} as found by Mazzali et al. (2002).

This plot shows that the Fe II λ5169 line cannot be used to accurately define the velocity of Fe II in blended lines, and if one is to use this line in this respect then appropriate steps must be taken to quantify the uncertainties. The inclusion of v_{ph} also demonstrates that Fe II λ5169 is a poor proxy for the photospheric velocity.

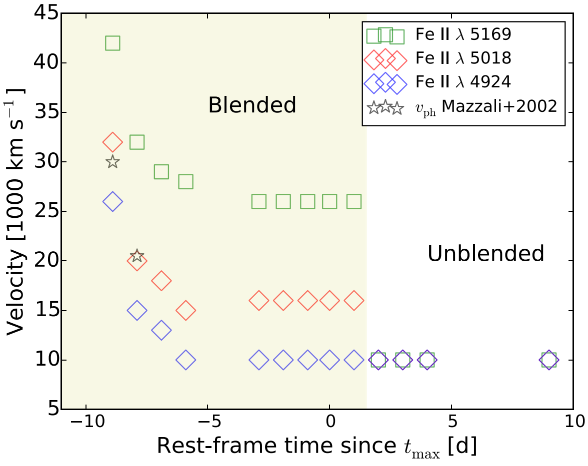

Figure B1. The line velocity of the absorption feature at ∼4800 Å in SN 2002ap as measured using three iron lines; Fe II λλ4924, 5018, 5169. The periods when the lines are blended and clearly unblended are marked. We also include the photospheric velocity measurements determined through spectral modelling (Mazzali et al. 2002). It can be see that Fe II λ5169 is a poor proxy for the line velocity at peak because when the lines de-blend the velocity measurements are suddenly some ∼20 000 km s^{-1} lower. It may be tempting to use Fe II λ4924, as it appears to match the line velocity at the de-blending stage; however, at early times, this line returns velocities below that of the photospheric velocity, a situation that not physical.

APPENDIX C: SPECTRAL PLOTS

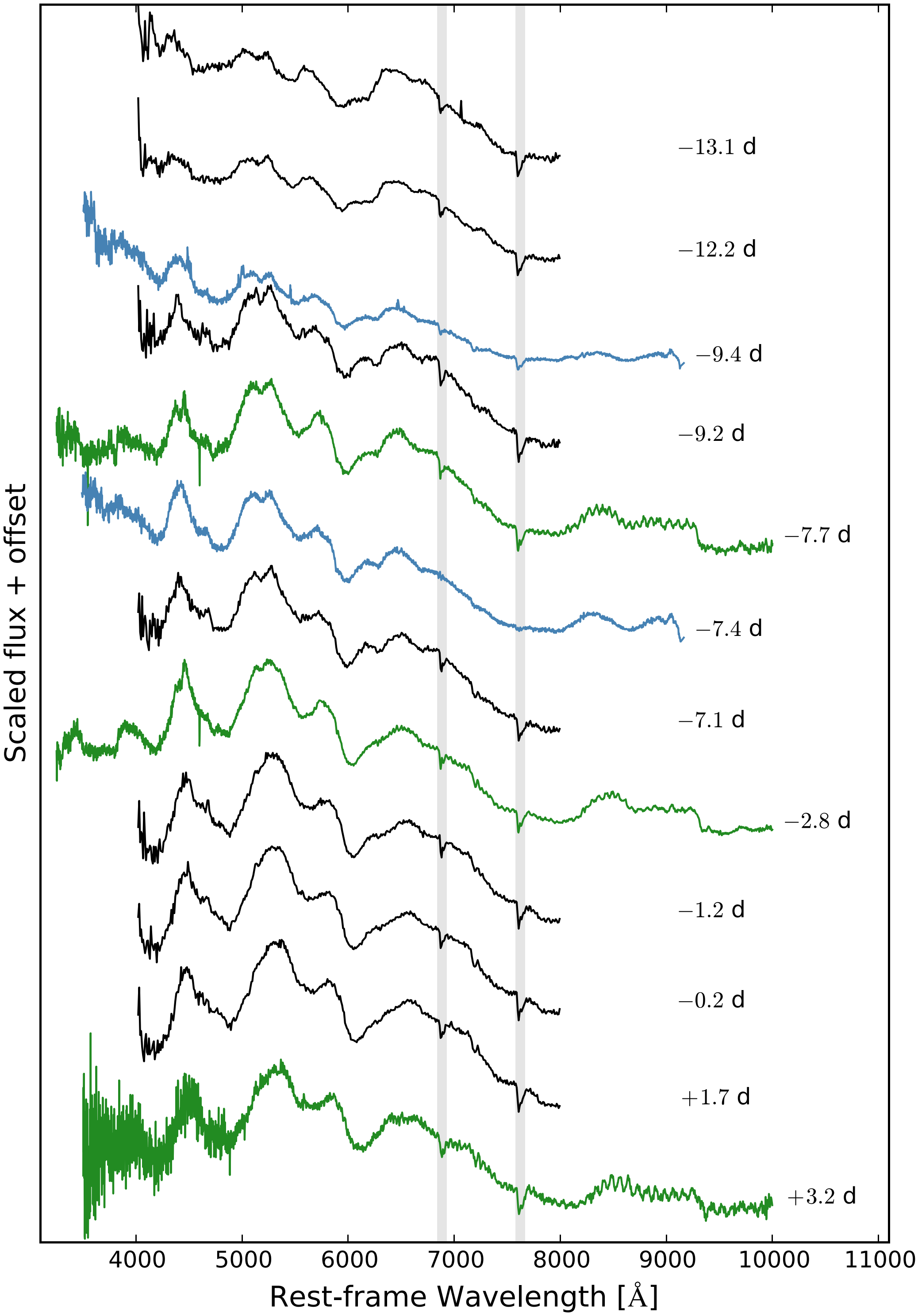

Figure C1. Extinction corrected spectra of SN 2016coi. The grey shaded regions represent prominent telluric features. Spectra are from LT (black), LJT (blue), LCO (green). In certain cases spectra have been truncated to remove excessive noise.

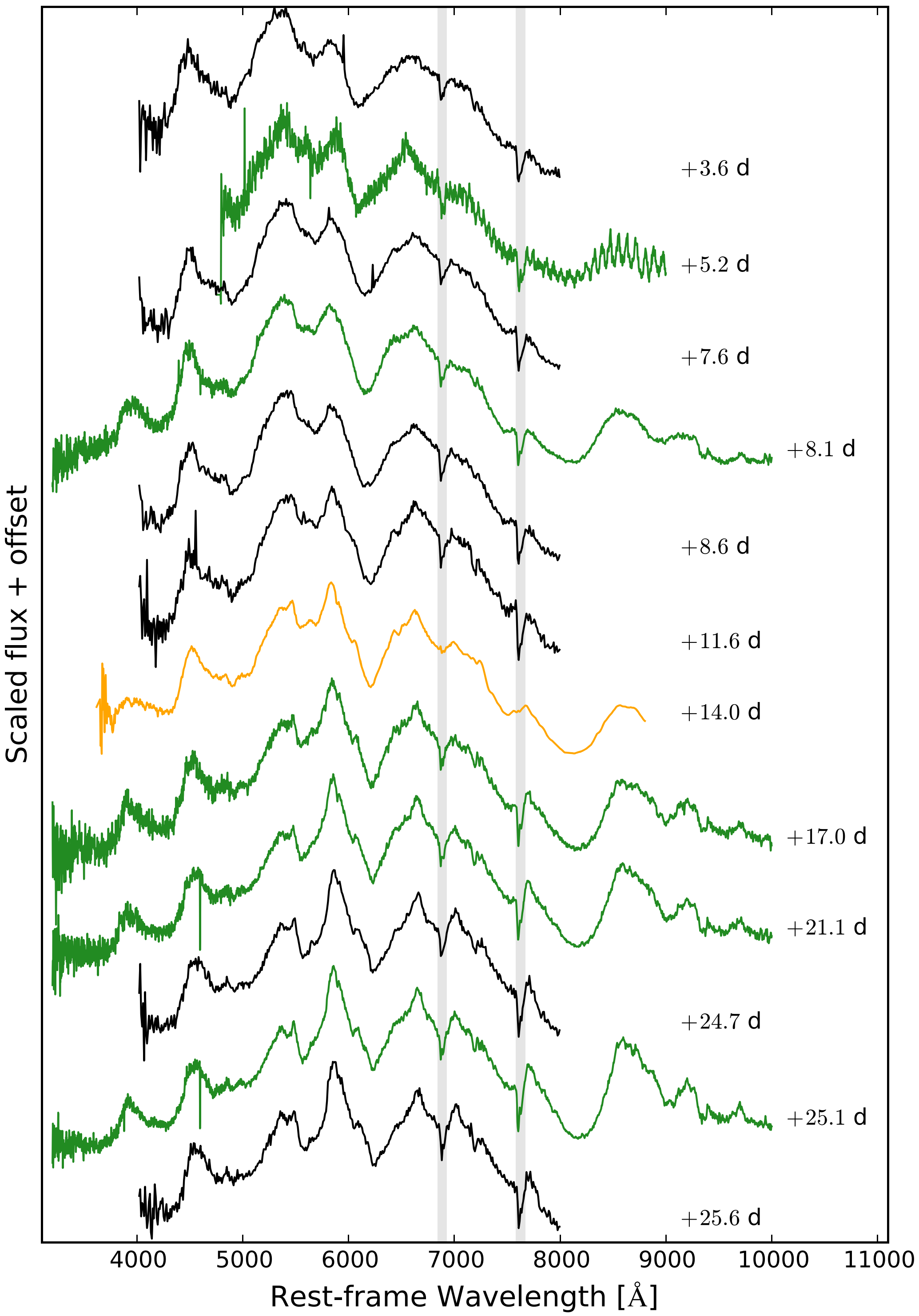

Figure C2. As Fig. C1. Additional spectra from Xianglong (orange).

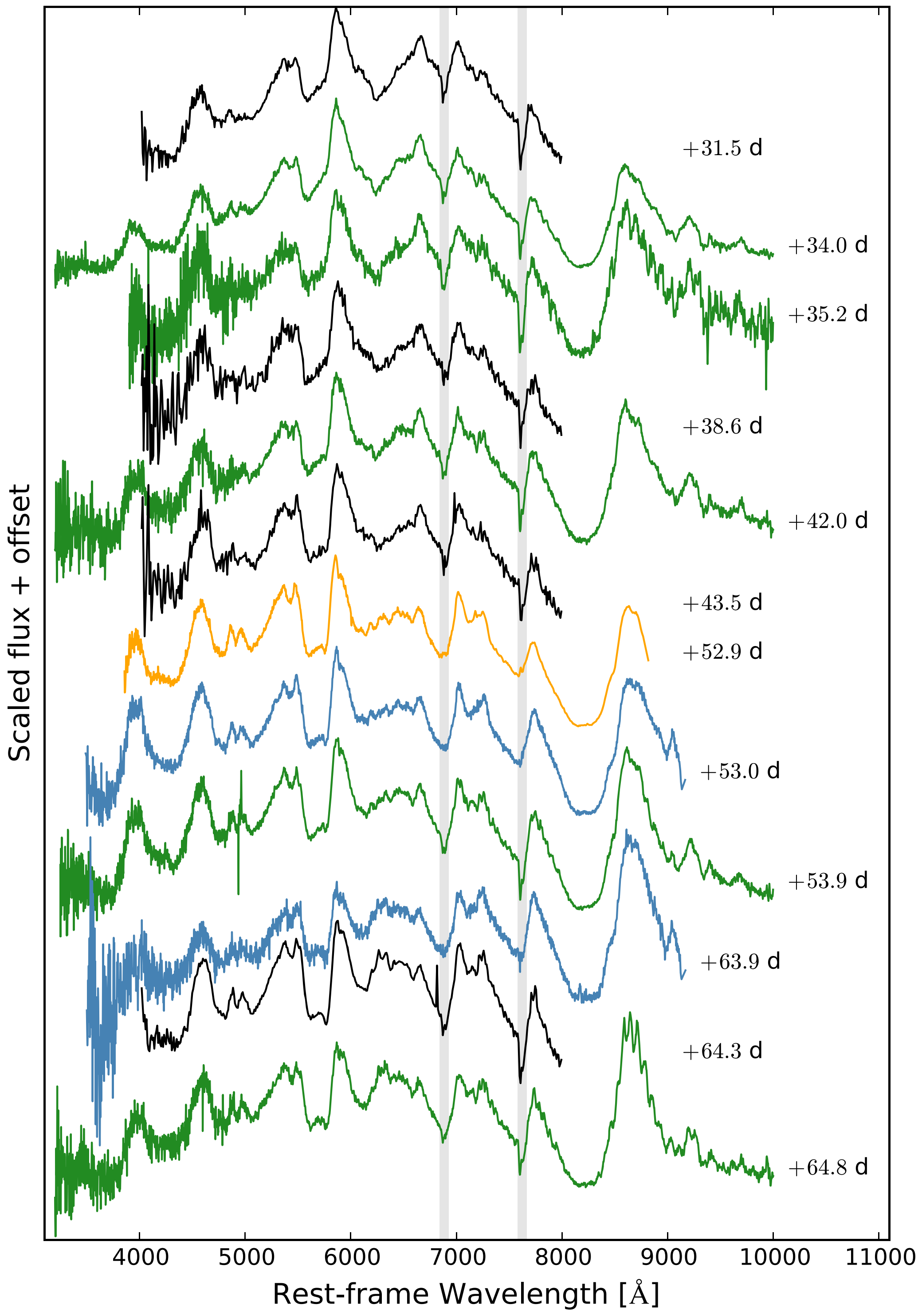

Figure C3. As Fig. C1.

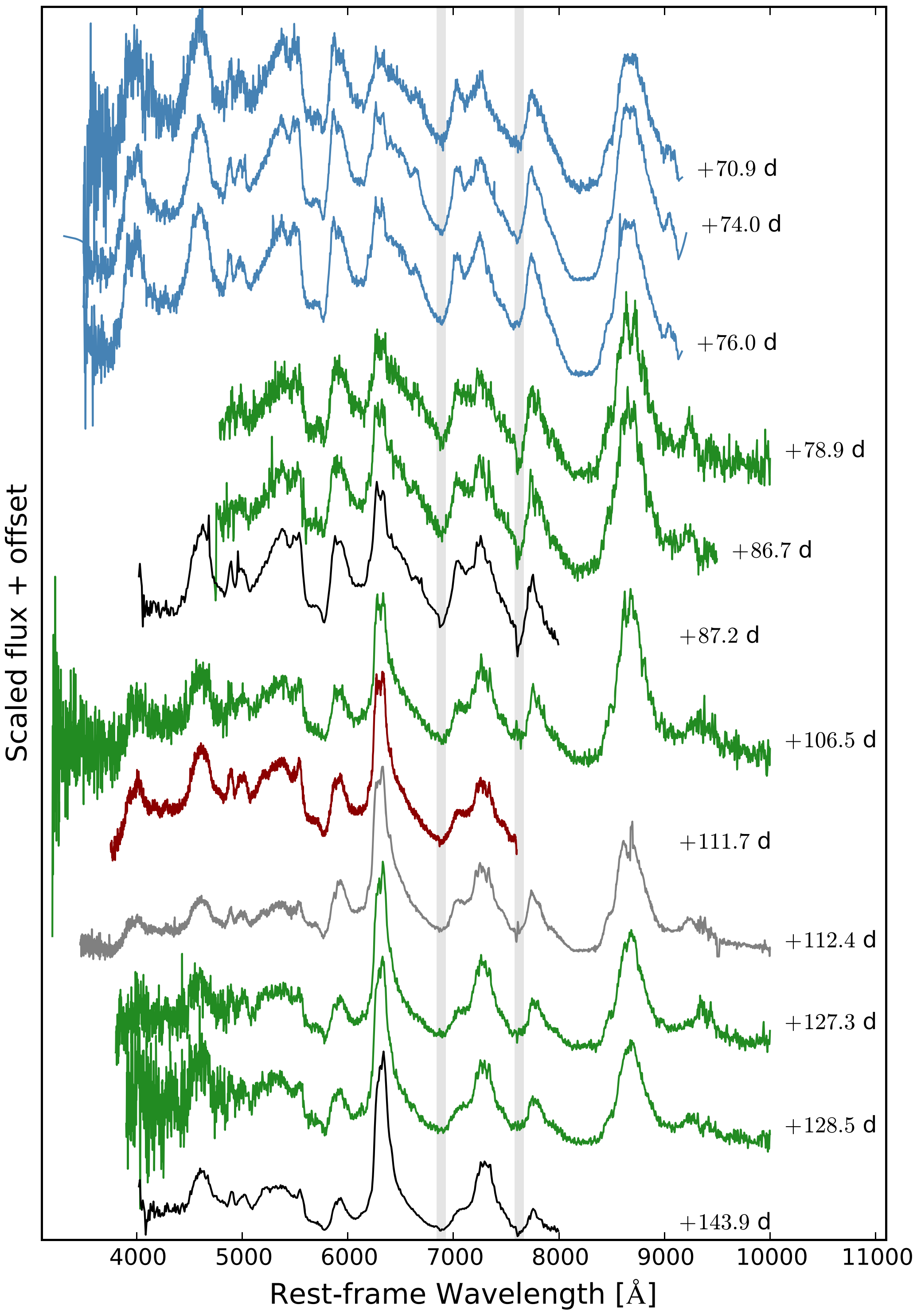

Figure C4. As Fig. C1. Additional spectra from the INT (dark red) and Lick (grey).

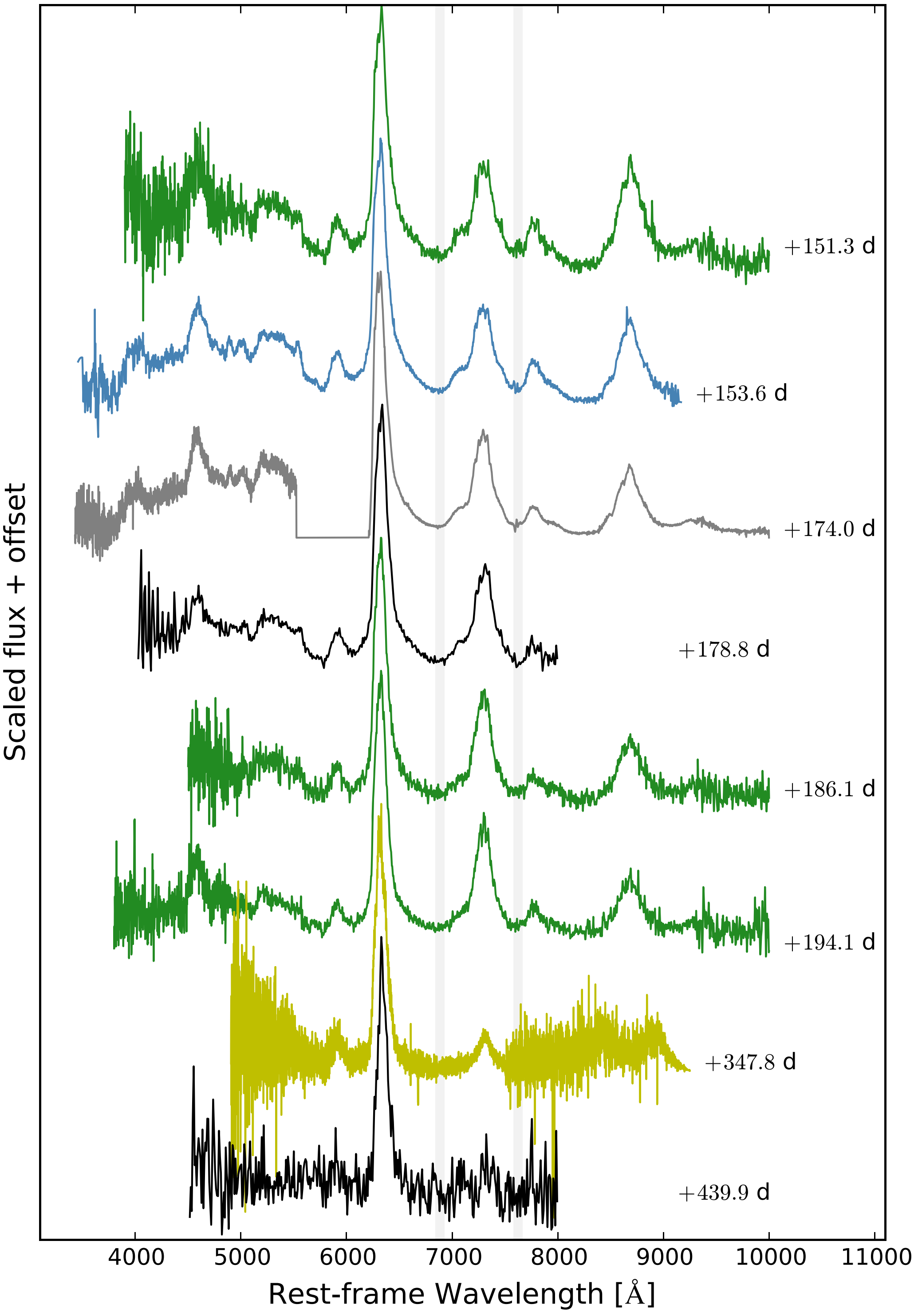

Figure C5. As Fig. C1. The DEIMOS spectrum is in yellow.

APPENDIX D: TABLES

Table D1. Journal of spectroscopic observations.

MJD	$t - t_{\max}$ (Rest-frame d)	Telescope	Wavelength range* (Å)	Exposure time (s)
57536.19	− 13.1	LT	4000–8000	200
57537.13	− 12.2	LT	4000–8000	100
57539.88	− 9.5	LJT	3500–9200	1800
57540.11	− 9.2	LT	4000–8000	100
57541.59	− 7.8	LCO (Haleakala)	3200–10 000	1200
57541.87	− 7.5	LJT	3500–9200	1800
57542.17	− 7.2	LT	4000–8000	100
57546.56	− 2.8	LCO (Haleakala)	3200–10 000	1200
57548.14	− 1.2	LT	4000–8000	100
57549.15	− 0.2	LT	4000–8000	100
57551.14	1.6	LT	4000–8000	100
57552.67	3.2	LCO (SSO)	3200–10 000	1200
57553.07	3.6	LT	4000–8000	100
57554.67	5.2	LCO (SSO)*	3200–10 000	400
57557.11	7.6	LT	4000–8000	100
57557.53	8.0	LCO (Haleakala)	3200–10 000	1200
57558.07	8.6	LT	4000–8000	100
57561.04	11.5	LT	4000–8000	100
57563.74	14.2	XLT	3600–8800	2400
57566.51	17.0	LCO (Haleakala)	3200–10 000	1200
57570.59	21.0	LCO (Haleakala)	3200–10 000	1200
57574.20	24.6	LT	4000–8000	150
57574.59	25.0	LCO (Haleakala)	3200–10 000	1200
57575.14	25.6	LT	4000–8000	150
57581.01	31.4	LT	4000–8000	150
57583.59	34.0	LCO (Haleakala)	3200–10 000	1800
57584.72	35.1	LCO (SSO)	3200–10 000	1800
57588.14	38.5	LT	4000–8000	200
57591.58	41.9	LCO (Haleakala)	3200–10 000	1800
57593.12	43.5	LT	4000–8000	300
57602.65	53.0	XLT	3600–8800	2700
57602.68	53.0	LJT	3500–9200	1800
57603.53	53.9	LCO (Haleakala)	3200–10 000	1800
57613.59	63.9	LJT	3500–9200	2700
57613.93	64.2	LT	4000–8000	1000
57614.47	64.7	LCO (Haleakala)	3200–10 000	1800
57620.57	70.8	LJT	3500–9200	2700
57623.69	73.9	LJT	3500–9200	2700
57625.66	75.9	LJT	3500–9200	2700
57628.62	78.8	LCO (SSO)*	3200–10 000	1500
57636.50	86.7	LCO (Haleakala)*	3200–10 000	1500
57636.99	87.2	LT	4000–8000	700
57656.36	106.5	LCO (Haleakala)	3200–10000	1800
57661.5	111.6	INT	3700–7600	3600
57662.20	112.3	Lick	3400–10 000	2700
57677.20	127.3	LCO (Haleakala)	3200–10 000	1800
57678.41	128.5	LCO (Haleakala)	3200–10 000	1800
57693.84	143.8	LT	4000–8000	1500
57701.32	151.3	LCO (Haleakala)	3200–10 000	1800
57703.57	153.5	LJT	3500–9200	2400
57724.11	174.0	Lick	3400–10 000	1200
57728.84	178.7	LT	4000–8000	1500
57736.23	186.1	LCO (Haleakala)	3200–10 000	1800
57744.21	194.0	LCO (Haleakala)	3200–10 000	1800
57898.5	347.8	Keck	4000–10 500	900
57990.94	439.9	LT	4000–8000	2400

*Denotes LCO data obtained independently of SNEx.

Table D2. *ugriz* observations of SN 2016coi.

MJD	u	δu	g	δg	r	δr	i	δi	z	δz	Telescope
57537.07	–	–	15.554	0.012	14.956	0.006	15.258	0.01	–	–	LCO (SAAO)
57537.11	–	–	15.555	0.007	14.962	0.004	15.266	0.002	–	–	LT
57538.12	–	–	15.255	0.002	14.695	0.002	15.011	0.008	14.933	0.001	LT
57539.12	–	–	14.988	0.007	14.479	0.009	14.839	0.018	–	–	LCO (SAAO)
57539.83	15.869	0.013	14.899	0.001	14.383	0.001	14.755	0.002	14.591	0.001	LJT
57540.14	15.731	0.013	14.804	0.003	14.281	0.002	14.669	0.001	14.541	0.002	LT
57541.86	–	–	14.649	0.012	14.152	0.004	14.551	0.003	14.342	0.010	LJT
57542.12	–	–	14.511	0.006	14.028	0.002	14.418	0.006	–	–	LCO (SAAO)
57542.16	15.633	0.005	14.511	0.001	14.028	0.001	14.421	0.001	14.25	0.001	LT
57544.50	–	–	14.235	0.005	13.814	0.002	14.206	0.003	–	–	LCO (Haleakala)*
57545.11	–	–	14.251	0.011	13.747	0.005	14.162	0.008	–	–	LCO (SAAO)
57548.17	15.767	0.006	14.171	0.001	13.749	0.001	14.037	0.001	13.78	0.001	LT
57549.16	15.747	0.013	14.176	0.001	13.609	0.002	14.019	0.001	13.729	0.002	LT
57551.13	15.923	0.018	14.186	0.007	13.571	0.002	13.971	0.002	13.666	0.003	LT
57552.07	–	–	14.015	0.002	13.432	0.005	–	–	–	–	LCO (SAAO)
57552.56	–	–	14.192	0.002	13.541	0.001	13.940	0.001	–	–	LCO (Haleakala)*
57553.08	16.186	0.014	14.251	0.010	13.594	0.003	13.947	0.002	13.622	0.006	LT
57557.11	16.647	0.032	14.485	0.014	13.633	0.004	13.957	0.001	13.629	0.002	LT
57557.16	–	–	14.468	0.012	13.618	0.009	–	–	–	–	LCO (SAAO)
57558.08	16.729	0.058	14.555	0.002	13.667	0.003	13.972	0.001	13.633	0.001	LT
57561.03	–	–	14.750	0.012	13.790	0.005	14.041	0.005	13.713	0.011	LT
57561.14	–	–	14.764	0.011	13.749	0.012	13.977	0.007	–	–	LCO (SAAO)
57564.16	–	–	14.999	0.080	13.887	0.011	14.093	0.007	–	–	LCO (SAAO)
57567.60	–	–	15.337	0.005	14.037	0.001	14.196	0.002	–	–	LCO (Haleakala)*
57568.11	–	–	15.285	0.012	14.092	0.004	14.253	0.005	13.874	0.005	LT
57568.15	–	–	15.269	0.008	14.066	0.011	14.212	0.005	–	–	LCO (SAAO)
57570.40	–	–	15.482	0.004	14.171	0.001	14.272	0.002	–	–	L57611.65
57574.13	–	–	15.616	0.006	14.34	0.005	–	–	–	–	LCO (SAAO)
57574.19	–	–	15.654	0.005	14.390	0.001	14.467	0.001	14.055	0.001	LT
57576.38	–	–	15.77	0.006	14.444	0.001	14.493	0.002	–	–	LCO (Haleakala)*
57576.41	–	–	15.723	0.003	14.423	0.003	14.487	0.004	–	–	LCO (CTIO)
57579.07	–	–	15.8	0.007	14.587	0.002	14.619	0.002	14.159	0.003	LT
57579.60	–	–	–	–	14.641	0.005	14.658	0.011	–	–	LCO (SSO)*
57581.10	–	–	15.875	0.007	14.634	0.004	14.654	0.004	–	–	LCO (SAAO)
57582.36	–	–	16.041	0.012	14.705	0.003	14.689	0.003	–	–	LCO (Haleakala)*
57586.13	–	–	16.022	0.002	14.850	0.002	14.828	0.004	14.317	0.001	LT
57587.09	–	–	16.049	0.004	14.883	0.002	14.865	0.001	14.337	0.001	LT
57587.11	–	–	16.061	0.014	14.885	0.007	14.844	0.007	–	–	LCO (SAAO)
57591.55	–	–	–	–	15.026	0.007	14.952	0.006	–	–	LCO (Haleakala)*
57593.14	–	–	16.169	0.004	15.052	0.002	15.014	0.001	14.458	0.001	LT
57594.73	–	–	16.193	0.008	15.087	0.005	15.034	0.006	–	–	LCO (SSO)
57596.44	–	–	16.27	0.009	15.107	0.002	15.069	0.003	–	–	LCO (Haleakala)*
57601.32	–	–	16.284	0.005	15.225	0.004	15.141	0.005	–	–	LCO (CTIO)
57602.67	–	–	16.375	0.001	15.333	0.001	15.266	0.001	14.637	0.001	LJT
57605.54	–	–	16.344	0.008	15.324	0.003	15.224	0.004	–	–	LCO (Haleakala)*
57606.52	–	–	16.357	0.007	15.34	0.003	15.255	0.004	–	–	LCO (Haleakala)*
57609.01	–	–	16.419	0.009	15.417	0.002	15.352	0.001	14.692	0.002	LT
57611.65	–	–	16.413	0.010	15.427	0.003	15.369	0.003	–	–	LCO (SSO)*
57613.58	–	–	16.491	0.006	15.543	0.001	15.481	0.001	14.787	0.001	LJT
57617.75	–	–	–	–	15.720	0.012	15.706	0.026	–	–	LJT
57620.03	–	–	16.552	0.010	15.631	0.003	15.536	0.001	14.864	0.004	LT
57620.56	–	–	–	–	15.617	0.003	15.54	0.002	–	–	LJT
57621.02	–	–	16.588	0.029	15.659	0.02	15.577	0.018	–	–	LCO (SAAO)
57622.64	–	–	16.673	0.005	15.733	0.002	15.679	0.001	14.977	0.004	LJT
57623.68	–	–	16.692	0.010	15.719	0.001	–	–	14.951	0.002	LJT
57625.02	–	–	16.621	0.001	15.706	0.001	15.619	0.001	14.925	0.001	LT
57620.19	–	–	16.531	0.0	15.637	0.0	15.546	0.0	–	–	LT
57620.56	–	–	–	–	15.617	0.003	15.54	0.002	–	–	LJT
57621.02	–	–	16.588	0.029	15.659	0.02	15.577	0.018	–	–	LCO (SAAO)
57622.64	–	–	16.673	0.005	15.733	0.002	15.679	0.001	14.977	0.004	LJT
57623.68	–	–	16.692	0.010	15.719	0.001	–	–	14.951	0.002	LJT
57625.65	–	–	16.654	0.003	15.746	0.001	–	–	–	–	LJT
57626.58	–	–	16.657	0.014	15.692	0.005	–	–	–	–	LCO (Haleakala)

Table D2 – *continued*

MJD	u	δu	g	δg	r	δr	i	δi	z	δz	Telescope
57627.97	–	–	16.609	0.012	15.74	0.008	15.638	0.009	–	–	LCO (SAAO)
57634.45	–	–	16.686	0.013	15.786	0.006	15.814	0.006	–	–	LCO (SSO)
57635.00	–	–	16.739	0.001	15.866	0.001	15.799	0.001	15.087	0.001	LT
57635.98	–	–	16.737	0.014	15.872	0.012	15.825	0.014	–	–	LCO (SAAO)
57636.00	–	–	16.755	0.003	15.874	0.001	15.817	0.001	15.114	0.002	LT
57638.98	–	–	16.798	0.001	15.928	0.001	15.878	0.001	15.134	0.001	LT
57641.93	–	–	16.831	0.002	15.966	0.001	15.92	0.001	15.209	0.001	LT
57642.94	–	–	16.796	0.015	15.999	0.01	15.945	0.012	–	–	LCO (SAAO)
57644.92	–	–	16.864	0.002	16.015	0.002	15.982	0.001	15.259	0.001	LT
57647.90	–	–	16.903	0.008	16.048	0.002	16.027	0.002	15.304	0.002	LT
57650.32	–	–	16.871	0.013	16.05	0.005	16.043	0.004	–	–	LCO (Haleakala)
57650.97	–	–	16.964	0.003	16.106	0.001	16.078	0.001	15.381	0.002	LT
57656.90	–	–	17.005	0.008	16.187	0.007	16.163	0.01	–	–	LCO (SAAO)
57657.26	–	–	16.988	0.016	16.172	0.007	16.174	0.007	–	–	LCO (Haleakala)
57660.90	–	–	–	–	16.38	0.101	16.294	0.087	–	–	LCO (SAAO)
57661.47	–	–	17.08	0.021	16.212	0.008	16.224	0.008	–	–	LCO (Haleakala)*
57667.87	–	–	17.191	0.008	16.343	0.001	16.348	0.001	15.683	0.002	LT
57672.91	–	–	17.26	0.001	16.402	0.001	16.426	0.001	15.781	0.001	LT
57676.45	–	–	17.266	0.087	16.409	0.064	16.464	0.069	–	–	LCO (SSO)*
57680.12	–	–	17.318	0.017	16.508	0.013	–	–	–	–	LCO (CTIO)
57683.46	–	–	17.395	0.008	16.527	0.006	16.556	0.008	–	–	LCO (SSO)
57685.43	–	–	17.423	0.002	16.509	0.001	16.576	0.001	–	–	LCO (SSO)*
57692.44	–	–	17.517	0.005	16.626	0.001	16.712	0.002	–	–	LCO (SSO)*
57696.29	–	–	17.565	0.001	16.671	0.001	16.814	0.003	–	–	LCO (Haleakala)*
57699.76	–	–	17.636	0.015	16.71	0.011	16.786	0.012	–	–	LCO (SAAO)
57701.81	–	–	17.716	0.003	16.751	0.003	16.865	0.001	16.418	0.003	LT
57702.69	–	–	–	–	16.847	0.004	16.938	0.005	–	–	LJT
57703.56	–	–	–	–	16.899	0.225	16.997	0.005	–	–	LJT
57710.25	–	–	18.018	0.234	16.819	0.016	16.852	0.047	–	–	LCO (Haleakala)*
57711.83	–	–	17.889	0.001	16.886	0.001	16.999	0.001	16.612	0.001	LT
57716.14	–	–	17.883	0.021	16.931	0.015	16.98	0.02	–	–	LCO (McDonald)
57717.40	–	–	18.076	0.006	16.952	0.005	17.043	0.002	–	–	LCO (SSO)*
57727.80	–	–	18.183	0.001	17.121	0.001	17.227	0.001	16.997	0.001	LT
57729.80	–	–	18.236	0.012	17.058	0.008	17.106	0.010	17.228	0.011	LT
57732.14	–	–	18.256	0.027	17.195	0.019	17.257	0.026	–	–	LCO (McDonald)
57732.80	–	–	18.28	0.002	17.202	0.002	17.296	0.001	17.127	0.005	LT
57732.81	–	–	18.283	0.002	17.204	0.001	17.313	0.001	17.133	0.004	LT
57736.82	–	–	18.375	0.003	17.27	0.001	17.373	0.022	17.239	0.001	LT
57758.08	–	–	18.71	0.035	17.575	0.021	17.720	0.028	–	–	LCO (McDonald)
57759.06	–	–	–	–	17.589	0.023	17.686	0.02	–	–	LCO (McDonald)
57898.79	–	–	20.893	0.05	19.403	0.028	19.942	0.049	–	–	LCO (SSO)
57914.37	–	–	20.888	0.118	19.598	0.051	20.134	0.062	–	–	LCO (CTIO)
57995.92	–	–	21.597	0.034	20.661	0.021	21.324	0.030	–	–	LT

*Denotes LCO data obtained independently of SNEx.

Table D3. *UBVRI* observations of SN 2016coi.

MJD	U	δU	B	δB	V	δV	R	δR	I	δI	Telescope
57536.98	–	–	15.958	0.073	15.314	0.044	14.875	0.036	14.912	0.024	Konkoly
57537.06	–	–	15.98	0.013	15.216	0.008	–	–	–	–	LCO (SAAO)
57539.12	–	–	15.501	0.010	14.661	0.017	–	–	–	–	LCO (SAAO)
57539.83	–	–	15.405	0.014	14.485	0.002	14.23	0.001	–	–	LJT
57540.02	–	–	15.31	0.095	14.506	0.051	14.159	0.042	14.256	0.021	Konkoly
57540.77	–	–	15.32	0.009	14.339	0.138	14.087	0.105	14.231	0.004	TNT
57541.75	14.9	0.021	15.15	0.005	14.16	0.004	13.92	0.005	14.077	0.006	TNT
57541.86	–	–	15.13	0.016	14.147	0.006	13.965	0.007	–	–	LJT
57542.12	–	–	15.076	0.004	14.13	0.003	–	–	–	–	LCO (SAAO)
57545.04	–	–	14.904	0.082	13.792	0.071	13.596	0.056	13.708	0.049	Konkoly
57545.10	–	–	14.907	0.005	13.876	0.006	–	–	–	–	LCO (SAAO)
57548.01	–	–	14.837	0.053	13.806	0.070	13.581	0.055	13.668	0.019	Konkoly
57549.72	–	–	14.859	0.004	13.698	0.003	13.447	0.003	13.572	0.004	TNT
57553.97	–	–	15.012	0.066	13.866	0.040	13.495	0.064	13.495	0.019	Konkoly
57557.15	–	–	15.287	0.006	13.893	0.003	–	–	–	–	LCO (SAAO)
57557.78	15.586	0.017	15.288	0.003	13.935	0.152	13.5	0.002	13.535	0.005	TNT
57558.04	–	–	15.454	0.117	13.954	0.084	13.505	0.063	13.569	0.080	Konkoly
57560.01	–	–	15.541	0.090	14.173	0.034	13.672	0.048	13.615	0.036	Konkoly
57561.04	–	–	15.656	0.182	14.199	0.041	13.656	0.066	13.553	0.039	Konkoly
57561.13	–	–	15.641	0.009	14.106	0.005	–	–	–	–	LCO (SAAO)
57562.05	–	–	15.775	0.104	14.266	0.089	13.816	0.102	13.573	0.047	Konkoly
57563.02	–	–	15.943	0.152	14.403	0.082	13.759	0.050	13.673	0.032	Konkoly
57564.15	–	–	15.903	0.015	14.299	0.006	–	–	–	–	LCO (SAAO)
57564.99	–	–	16.079	0.072	14.434	0.055	13.865	0.034	13.718	0.044	Konkoly
57568.14	–	–	16.174	0.011	14.552	0.005	–	–	–	–	LCO (SAAO)
57569.04	–	–	16.247	0.074	14.646	0.084	13.86	0.046	13.76	0.041	Konkoly
57570.98	–	–	16.237	0.138	14.727	0.065	13.835	0.078	13.773	0.065	Konkoly
57572.12	–	–	16.468	0.025	14.794	0.006	–	–	–	–	LCO (SAAO)
57573.98	–	–	16.457	0.054	14.919	0.071	14.171	0.031	13.999	0.027	Konkoly
57574.13	–	–	16.491	0.013	14.907	0.006	–	–	–	–	LCO (SAAO)
57574.70	17.065	0.046	16.424	0.008	14.935	0.005	14.172	0.003	13.993	0.004	TNT
57576.01	–	–	16.543	0.085	15.009	0.064	14.266	0.034	14.051	0.020	Konkoly
57576.40	–	–	16.588	0.009	15.004	0.004	–	–	–	–	LCO (CTIO)
57578.97	–	–	16.602	0.066	15.15	0.049	14.386	0.041	14.153	0.036	Konkoly
57579.98	–	–	16.629	0.097	15.178	0.049	14.472	0.066	14.186	0.034	Konkoly
57581.09	–	–	16.724	0.011	15.172	0.005	–	–	–	–	LCO (SAAO)
57587.11	–	–	16.901	0.141	15.396	0.015	–	–	–	–	LCO (SAAO)
57594.73	–	–	16.981	0.019	15.575	0.007	–	–	–	–	LCO (SSO)
57601.32	–	–	17.085	0.011	15.724	0.005	–	–	–	–	LCO (CTIO)
57602.67	–	–	–	–	15.77	1.776	15.055	0.003	–	–	LJT
57603.86	–	–	16.984	0.061	15.806	0.047	15.072	0.036	14.618	0.036	Konkoly
57603.90	–	–	17.069	0.091	15.795	0.053	15.071	0.036	14.647	0.028	Konkoly
57609.00	–	–	17.233	0.021	15.888	0.01	–	–	–	–	LCO (SAAO)
57613.00	–	–	17.139	0.065	15.953	0.064	15.27	0.037	14.783	0.021	Konkoly
57613.58	–	–	17.203	0.010	15.972	0.003	15.28	0.003	–	–	LJT
57617.75	–	–	17.09	0.040	16.058	0.014	15.275	0.058	–	–	LJT
57620.56	–	–	–	–	16.109	0.001	15.424	0.001	–	–	LJT
57621.01	–	–	17.205	0.061	16.022	0.032	–	–	–	–	LCO (SAAO)
57622.64	–	–	17.29	0.001	16.11	0.001	15.426	0.003	14.857	0.001	LJT
57623.68	–	–	17.302	0.012	16.118	0.003	15.444	0.001	–	–	LJT
57625.65	–	–	17.313	0.013	16.143	0.002	15.479	0.001	–	–	LJT
57625.90	–	–	17.238	0.085	16.165	0.041	15.501	0.046	15.003	0.025	Konkoly
57627.97	–	–	17.369	0.032	16.151	0.014	–	–	–	–	LCO (SAAO)
57631.88	–	–	17.329	0.073	16.234	0.049	15.625	0.054	15.088	0.040	Konkoly
57638.89	–	–	17.367	0.062	16.391	0.050	15.702	0.038	15.192	0.014	Konkoly
57642.94	–	–	17.565	0.041	16.387	0.016	–	–	–	–	LCO (SAAO)
57646.78	–	–	17.544	0.173	16.483	0.072	15.807	0.028	15.346	0.040	Konkoly
57649.92	–	–	17.435	0.083	16.503	0.031	–	–	–	–	LCO (SAAO)
57654.75	–	–	17.564	0.128	16.544	0.102	15.916	0.057	15.423	0.033	Konkoly
57656.89	–	–	17.724	0.027	16.595	0.011	–	–	–	–	LCO (SAAO)
57660.81	–	–	17.639	0.048	16.709	0.066	16.031	0.034	15.577	0.028	Konkoly
57668.68	–	–	17.891	0.017	16.848	0.016	16.142	0.01	15.687	0.01	TNT
57669.53	–	–	17.805	0.012	16.807	0.01	16.11	0.007	15.661	0.007	TNT
57670.50	–	–	17.831	0.011	16.84	0.011	16.146	0.007	15.667	0.007	TNT

Table D3 – *continued*

MJD	*U*	δ*U*	*B*	δ*B*	*V*	δ*V*	*R*	δ*R*	*I*	δ*I*	Telescope
57671.53	–	–	–	–	16.916	0.029	16.143	0.016	15.683	0.012	TNT
57680.11	–	–	18.076	0.041	17.020	0.022	–	–	–	–	LCO (CTIO)
57683.46	–	–	18.023	0.015	17.04	0.01	–	–	–	–	LCO (SSO)
57683.72	–	–	17.935	0.088	17.109	0.051	16.316	0.030	15.948	0.027	Konkoly
57684.51	–	–	–	–	17.083	0.046	16.35	0.015	15.896	0.093	TNT
57685.64	–	–	18.074	0.028	17.133	0.018	16.369	0.009	15.978	0.128	TNT
57686.54	–	–	18.192	0.022	17.164	0.011	–	–	16	0.007	TNT
57687.57	–	–	–	–	17.184	0.096	–	–	–	–	TNT
57692.48	–	–	18.181	0.016	17.209	0.014	16.443	0.010	16.072	0.009	TNT
57696.52	–	–	18.196	0.021	17.273	0.01	–	–	16.107	0.008	TNT
57697.46	–	–	18.29	0.024	17.305	0.017	16.527	0.009	16.154	0.01	TNT
57699.46	–	–	–	–	17.305	0.035	16.489	0.019	16.093	0.026	TNT
57699.75	–	–	18.374	0.036	17.280	0.02	–	–	–	–	LCO (SAAO)
57700.49	–	–	–	–	17.362	0.013	16.536	0.007	16.2	0.009	TNT
57702.53	–	–	–	–	17.377	0.024	16.565	0.014	–	–	TNT
57703.56	–	–	18.407	0.004	17.435	0.002	16.587	0.003	–	–	LJT
57704.48	–	–	–	–	17.501	0.048	16.48	0.023	–	–	TNT
57706.42	–	–	18.41	0.041	17.449	0.025	16.6	0.013	20.350	0.014	TNT
57706.73	–	–	18.308	0.082	17.566	0.067	16.598	0.060	16.297	0.048	Konkoly
57707.44	–	–	–	–	17.456	0.036	16.624	0.014	–	–	TNT
57708.42	–	–	18.48	0.02	17.547	0.014	16.679	0.007	16.373	0.008	TNT
57711.52	–	–	18.530	0.040	17.647	0.309	16.687	0.018	16.395	0.019	TNT
57713.76	–	–	18.415	0.045	17.615	0.030	16.685	0.037	16.443	0.028	Konkoly
57714.45	–	–	18.271	0.362	17.452	0.066	16.679	0.058	16.403	0.034	TNT
57715.44	–	–	18.536	0.034	17.635	0.027	16.694	0.014	16.442	0.017	TNT
57716.02	–	–	–	–	17.596	0.036	–	–	–	–	LCO (CTIO)
57716.14	–	–	18.574	0.025	17.612	0.023	–	–	–	–	LCO (McDonald)
57716.56	–	–	–	–	17.677	0.016	16.721	0.009	16.463	0.010	TNT
57718.43	–	–	18.522	0.016	17.693	0.014	16.77	0.008	16.494	0.01	TNT
57719.49	–	–	18.543	0.023	17.697	0.018	16.806	0.008	16.525	0.019	TNT
57720.46	–	–	18.59	0.012	17.739	0.011	–	–	16.537	0.007	TNT
57722.46	–	–	18.641	0.020	17.765	0.017	16.834	0.007	–	–	TNT
57723.42	–	–	18.633	0.025	17.796	0.023	16.854	0.014	16.587	0.016	TNT
57725.67	–	–	18.668	0.108	17.88	0.052	16.834	0.065	16.625	0.035	Konkoly
57732.13	–	–	18.836	0.069	17.969	0.047	–	–	–	–	LCO (McDonald)
57738.75	–	–	18.887	0.100	18.193	0.061	17.047	0.047	16.906	0.028	Konkoly
57744.70	–	–	18.942	0.056	18.333	0.049	17.175	0.037	16.95	0.031	Konkoly
57759.06	–	–	19.092	0.051	18.462	0.049	–	–	–	–	LCO (McDonald)
57774.70	–	–	19.294	0.158	18.97	0.106	17.582	0.070	17.435	0.062	Konkoly

Table D4. DLT40 open filter (scaled to *r*) observations of SN 2016coi.

MJD	Open(*r*)	δ Open(*r*)	Telescope
57555.39	13.822	0.061	DLT40
57557.38	13.879	0.090	DLT40
57558.38	13.917	0.077	DLT40
57559.37	13.937	0.069	DLT40
57561.42	14.052	0.040	DLT40
57562.38	14.089	0.093	DLT40
57566.39	14.269	0.048	DLT40
57568.38	14.364	0.055	DLT40
57569.41	14.389	0.042	DLT40
57575.34	14.612	0.051	DLT40
57576.38	14.654	0.058	DLT40
57577.35	14.730	0.055	DLT40
57584.30	14.911	0.067	DLT40
57585.32	14.967	0.079	DLT40
57589.40	15.062	0.067	DLT40
57590.29	15.081	0.076	DLT40
57591.29	15.095	0.122	DLT40
57592.38	15.116	0.064	DLT40
57595.32	15.182	0.049	DLT40
57597.27	15.255	0.061	DLT40
57598.31	15.265	0.084	DLT40
57599.26	15.295	0.066	DLT40
57600.29	15.315	0.046	DLT40
57601.25	15.345	0.089	DLT40
57602.25	15.360	0.064	DLT40
57603.25	15.357	0.059	DLT40
57605.24	15.414	0.074	DLT40
57606.24	15.424	0.041	DLT40
57607.23	15.433	0.063	DLT40
57608.23	15.466	0.064	DLT40
57609.23	15.468	0.068	DLT40
57610.23	15.494	0.088	DLT40
57612.22	15.529	0.061	DLT40
57611.22	15.491	0.057	DLT40
57613.22	15.539	0.080	DLT40
57614.22	15.555	0.053	DLT40
57615.21	15.550	0.066	DLT40
57616.21	15.571	0.065	DLT40
57617.12	15.596	0.063	DLT40
57618.21	15.620	0.074	DLT40
57619.20	15.597	0.090	DLT40
57620.20	15.534	0.067	DLT40
57621.20	15.653	0.071	DLT40
57622.2	15.624	0.054	DLT40
57625.27	15.716	0.087	DLT40
57626.25	15.738	0.055	DLT40
57629.21	15.733	0.042	DLT40
57630.21	15.792	0.059	DLT40
57631.20	15.791	0.068	DLT40
57632.21	15.857	0.095	DLT40
57634.12	15.829	0.070	DLT40
57635.12	15.853	0.072	DLT40
57637.23	15.890	0.059	DLT40
57638.06	15.914	0.052	DLT40
57639.06	15.925	0.083	DLT40
57640.06	15.924	0.056	DLT40
57642.06	15.969	0.067	DLT40
57643.05	15.976	0.051	DLT40
57644.03	16.008	0.115	DLT40
57645.08	16.078	0.087	DLT40
57647.03	16.071	0.054	DLT40
57648.02	16.081	0.046	DLT40
57649.01	16.055	0.039	DLT40
57650.11	16.053	0.032	DLT40

Table D4 – *continued*

MJD	Open(r)	δ Open(r)	Telescope
57651.02	16.037	0.048	DLT40
57652.02	16.073	0.041	DLT40
57653.04	16.110	0.050	DLT40
57654.03	16.145	0.049	DLT40
57655.03	16.178	0.052	DLT40
57656.03	16.170	0.051	DLT40
57657.02	16.188	0.033	DLT40
57658.03	16.255	0.046	DLT40
57659.11	16.269	0.045	DLT40
57660.07	16.169	0.040	DLT40
57661.02	16.252	0.046	DLT40
57662.02	16.302	0.047	DLT40
57663.02	16.287	0.053	DLT40
57664.02	16.292	0.041	DLT40
57666.02	16.337	0.036	DLT40
57667.02	16.304	0.044	DLT40
57668.02	16.329	0.047	DLT40
57669.02	16.406	0.038	DLT40
57670.08	16.330	0.054	DLT40
57671.01	16.453	0.039	DLT40
57672.03	16.445	0.039	DLT40
57673.01	16.449	0.055	DLT40
57675.01	16.452	0.047	DLT40
57676.01	16.435	0.051	DLT40

This paper has been typeset from a TEX/LATEX file prepared by the author.